JET

Journal of ENERGY TECHNOLOGY

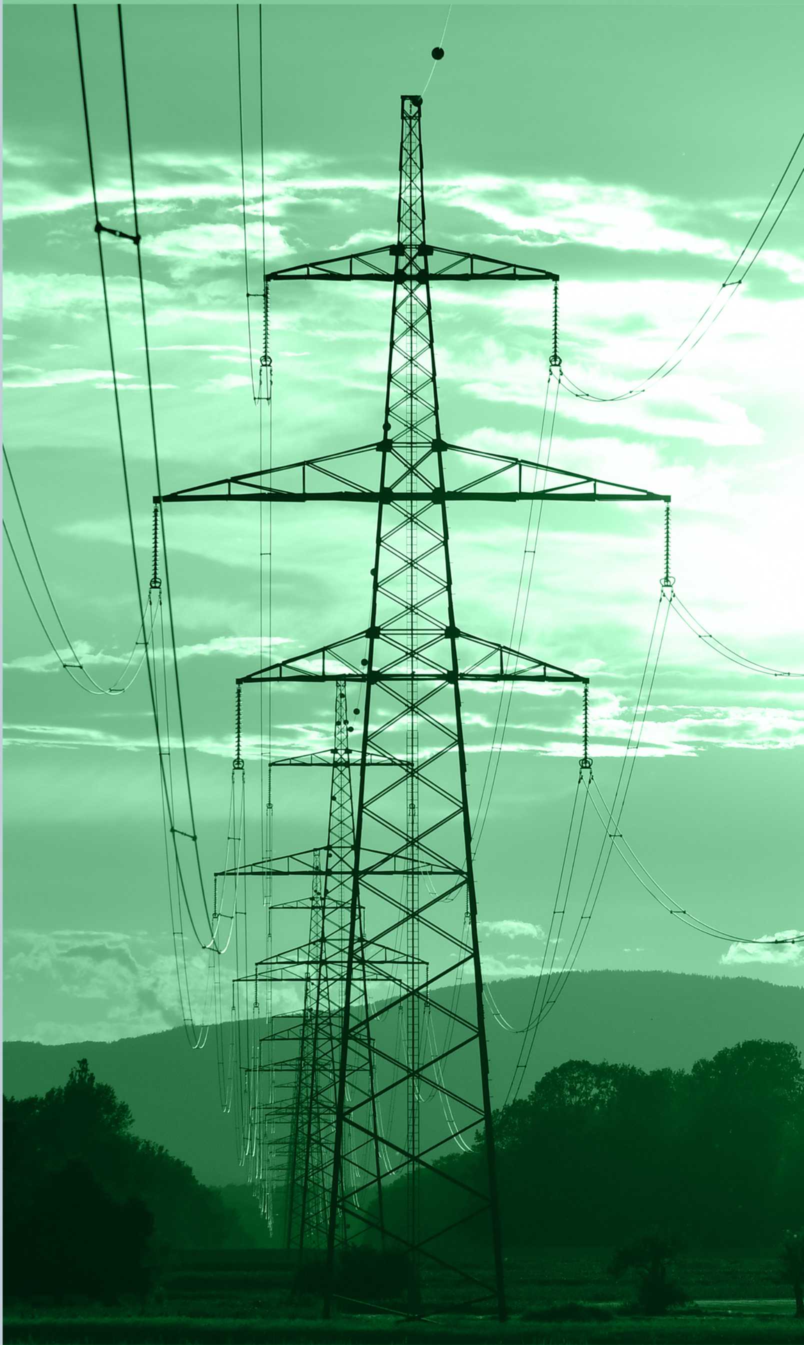

University of Maribor Press

VOLUME 18
ISSUE 4
DECEMBER 2025


JET

EDITORIAL OFFICE ADDRESS
University of Maribor
Faculty of Energy Technology
Hočevarjev trg 1, 8270 Krško, Slovenia
Koroška cesta 62a, 3320 Velenje, Slovenia
e-mail: jet@um.si
https://www.fe.um.si

PUBLISHED BY
University of Maribor
University Press
Slomškov trg 15, 2000 Maribor, Slovenia
e-mail: zalozba@um.si, zalozba.journals@um.si
https://press.um.si/
https://journals.um.si

EDITORIAL BOARD

Antun Barac (University of Slavonski Brod, Croatia) • Miloš Bekovič (University of Maribor, Slovenia) • Anton Bergant (Litostroj Power d.d., Slovenia) • Marinko Barukčić (Josip Juraj Strossmayer University of Osijek, Croatia) • Goga Cvetkovski (Ss. Cyril and Methodius University in Skopje, Macedonia) • Nenad Cvetković (University of Nis, Serbia) • Damir Dović (University of Zagreb, Croatia) • Željko Hederić (Josip Juraj Strossmayer University of Osijek, Croatia) • Dalibor Igrec (Margento R&D d.o.o., Slovenia) • Marko Jesenik (University of Maribor, Slovenia) • Eva Klemenčič (University of Maribor, Slovenia) • Ivan Aleksander Kodeli (Jožef Stefan Institute, Slovenia) • Ankica Kovač (University of Zagreb, Croatia) • Marjan Kromar (Jožef Stefan Institute, Slovenia) • Igor Medved (Slovak University of Technology in Bratislava, Slovakia) • Matej Mencinger (University of Maribor, Slovenia) • Franjo Pranjić (University of Maribor, Slovenia) • Anita Praprotnik Brdnik (University of Maribor, Slovenia) • Dušan Strušnik (Energetika Ljubljana d.o.o., Slovenia) • Klemen Sredenšek (University of Maribor, Slovenia) • Urška Lavrenčič Štangar (University of Ljubljana, Slovenia) • Gorazd Štumberger (University of Maribor, Slovenia) • Anton Trnik (Constantine the Philosopher University in Nitra, Slovakia) • Mykhailo Zagirnyak (Kremenchuk Mykhailo Ostrohradskyi National University, Ukraine) • Marija Živić (University of Slavonski Brod, Croatia)

University of Maribor

Faculty of Energy Technology

ISSN 2463-7815 (electronic)
ISSN 1855-5748 (printed)

The **Journal of Energy Technology** is a peer-reviewed journal published in May, August, November and December by University of Maribor Press and issued by University of Maribor, Faculty of Energy Technology (Slovenia). The journal is indexed and abstracted in databases INSPEC©, Proquest and EBSCO. For more information, please visit our website at https://journals.um.si/index.php/jet

© University of Maribor, University of Maribor Press
/ *Univerza v Mariboru, Univerzitetna založba*

Text © Authors, 2025

This journal is licensed under the Creative Commons Attribution 4.0 International License.

This license allows reusers to distribute, remix, adapt, and build upon the material in any medium or format, so long as attribution is given to the creator. The license allows for commercial use.

Any third-party material in this journal is published under the book's Creative Commons licence unless indicated otherwise in the credit line to the material. If you would like to reuse any third-party material not covered by the journals's Creative Commons licence, you will need to obtain permission directly from the copyright holder.

https://creativecommons.org/licenses/by/4.0

University of Maribor Press

Slovenian Research and Innovation Agency

Journal of Energy Technology is co-funded by Slovenian Research and Innovation Agency

Journal of Energy Technology

Volume 18 Number 4 December 2025

ARTICLES

JOURNAL OF ENERGY TECHNOLOGY
Vol. 18, No. 4, December 2025

Editorial

JURIJ AVSEC
Editor-in-Chief

The twenty-first century brings to the forefront several fundamental challenges of modern society: health, and the provision of food, energy and water. At the same time, new fields of knowledge are developing in parallel, such as nanotechnologies, the development of advanced materials and the application of artificial intelligence. Water resources are essential for economic activity and everyday life, as they enable the supply of drinking water, irrigation in agriculture, and support for transport, energy production, tourism and the preservation of natural ecosystems. Moreover, water resources can also be used for the production of hydrogen, methanol, or similar energy carriers. It should be emphasised that humans are not the only inhabitants of the planet, and that water is equally vital for the survival of other living organisms and plants.

Slovenia is relatively rich in water resources; nevertheless, their sustainable and prudent management is essential. According to data from ELES, hydropower plants contributed 36% of electricity generation in 2024, although this share varies from year to year depending on the hydrological conditions. Globally, approximately 15% of electricity is generated from hydropower, which still represents the largest share among renewable energy sources worldwide.

For these reasons, the development of hydropower systems is of exceptional importance. Several interesting topics in this field can also be found in our journal.
Kind regards to all the readers.

Uvodnik

Enaindvajseto stoletje v ospredje postavlja tri temeljne izzive sodobne družbe: zdravje ter zagotavljanje hrane, energije in vode. Ob tem se vzporedno razvijajo nova znanja, kot so nanotehnologije, razvoj novih materialov in uporaba umetne inteligence. Vodni viri so ključni za delovanje gospodarstva in vsakdanje življenje, saj omogočajo oskrbo s pitno vodo, namakanje v kmetijstvu ter podporo prometu, energetiki, turizmu in ohranjanju naravnih ekosistemov. Nenazadnje lahko vodni viri služijo tudi pri pridobivanju vodika, metanola oziroma podobnih energentov. Poudariti je treba, da ljudje na planetu nismo sami in da vodo za svoj obstoj potrebujejo tudi druga živa bitja in rastline.

Slovenija je relativno bogata z vodnimi viri, kljub temu pa je z njimi treba upravljati preudarno. Po podatkih ELES-a so hidroelektrarne leta 2024 prispevale 36 % k proizvodnji električne energije; ta delež se od leta do leta nekoliko spreminja zaradi hidroloških razmer. Na svetovni ravni znaša delež električne energije, pridobljene iz vodne energije, približno 15 %, kar še vedno predstavlja največji delež med obnovljivimi viri energije.

Zato je razvoj hidroenergetskih sistemov izjemnega pomena. Nekaj zanimivih tematik s tega področja lahko najdemo tudi v naši reviji.

Lep pozdrav vsem bralcem.

JOURNAL OF ENERGY TECHNOLOGY
Vol. 18, No. 4, pp. 189–202, December 2025

Original Scientific Article

Submitted
24. 11. 2025

Accepted
2. 12. 2025

Published
31. 12. 2025

APPROXIMATE, NUMERICAL AND EXPERIMENTAL INVESTIGATIONS OF A WATER HAMMER IN VRHOVO BULB-TURBINE HYDROELECTRIC POWER PLANT

ANTON BERGANT,[1, 2] JOŠT PEKOLJ[1]
[1] Litostroj Power d.o.o., Ljubljana, Slovenia
anton.bergant@litostrojpower.eu, jost.pekolj@litostrojpower.eu
[2] University of Ljubljana, Faculty of Mechanical Engineering, Ljubljana, Slovenia
anton.bergant@fs.uni-lj.si

CORRESPONDING AUTHOR
anton.bergant@litostrojpower.eu

Abstract This paper investigates the effectiveness and accuracy of approximate and numerical water hammer models in the Slovenian lower Sava River hydroelectric power plants with bulb turbines. An approximate model is introduced first, followed by numerical rigid water hammer models. Comparisons of the computed and measured results are examined for the transient load case of an emergency shutdown in Vrhovo hydroelectric power plant. The water hammer is mitigated by adjusting the guide vane and runner blade closing/opening laws properly. The results show a good agreement between the approximate and numerical and measured results.

Keywords
hydroelectric power plant,
bulb turbine,
water hammer,
computation,
field test, comparison study

https://doi.org/10.18690/jet.18.4.189-202.2025

University of Maribor Press

1 Introduction

Hydroelectric power plants are flexible in both operation and energy storage (large water reservoirs) [1]. Both aspects are important for the stability of the electric power grid, due to the increasing share of variable renewable energy sources. This paper focuses on water hammer events in bulb turbine hydroelectric power plants located on the lower Sava River in Slovenia. The river flows through the Sava River basin, which is the largest basin in Slovenia and represents more than 50% of the national territory, but is the least utilised in terms of hydropower, with a total installed capacity of 230 MW [2]. The hydroelectric power plants (HEPPs) with bulb turbines on the lower Sava River are (from north to south): Vrhovo HEPP (1993, 3×11 MW) and Boštanj HEPP (2006, 3×10.9 MW). The completion of the hydropower cascade on the lower Sava River is under way (including the planned Mavčiče HEPP with three bulb turbines).

Variations in the discharge of a hydraulic turbine induce higher dynamic loads on the plant components, because of the water hammer phenomena [3, 4]. The consequences of water hammer can result in damage to the turbine and hydromechanical equipment (turbine blade failure), to elements of the flow-passage system (pipe rupture), or in operational disturbances (plant outage). For utility owners, this translates into increased costs associated with repairs, repeated maintenance activities and a decrease in electricity generation. Therefore, excessive water hammer-induced loads in hydroelectric power plants must be limited to the values prescribed by the relevant research and Standards [5, 6].

Water hammer in hydroelectric power plants with bulb turbines can be controlled within the prescribed limits through a combination of several methods [3, 6, 7]. One of the most effective methods is the modification of the operational regimes. This involves finding the most suitable combination of the guide vane and runner blade closing and opening laws. A two-speed or multi-speed guide vane servomotor closing ramp (with an added cushioning time) can, in many cases, improve the operational safety of the plant significantly. The next method is to install surge control devices in the system. For example, a draft tube gate can prevent the occurrence of runaway conditions in a bulb turbine. Similarly, the sluicing operation of the bulb turbines and installation of a by-pass valve can attenuate open channel waves during transient events. In essence, these devices modify the dynamic response of the plant component characteristics (for example, by increasing the effective inertia of the turbine unit rotating parts). Another method of water hammer protection is the redesign of the flow passage layout. The redesign may include changes to the conduit geometry, such as diameter and length, or repositioning of key system components (e.g., gates). Finally, the water hammer safety measure can be the limitation of the plant's operating range. This can be done by imposing restrictions on the discharge, gross head, or unit power, to reduce the magnitude of extreme water hammer loads.

The most common water hammer control device in bulb turbine hydroelectric power schemes is the turbine governor coupled to the guide vane and runner blade servomotor mechanisms [8, 9]. The control devices should operate smoothly in the following normal operating conditions [6]: turbine start-up, load acceptance, load reduction, load rejection under governor control and emergency shutdown. Emergency conditions occur when one of the safety elements fails, which can cause partial turbine runaway. The full-turbine runaway is considered as a catastrophic transient regime. It occurs when several safety elements fail in the most unfavourable way. Water hammer analysis should be performed for normal, emergency and catastrophic operating conditions [6].

The main aim of this study is to validate three different computational water hammer models, including an approximate model [10], and one-dimensional (1D) [11] and three-dimensional (3D) [12], [13] numerical rigid water hammer models. The results obtained from these simulations are then compared with the measurement data collected at the Vrhovo HEPP. Comparisons of the computed and measured results are examined for a normal operating transient regime.

2 Theoretical modelling

Hydraulic transients in hydroelectric power plants equipped with bulb turbines can be analysed using either the elastic [3, 7] or rigid [7, 11] water hammer theories. Run-of-river power plants comprise relatively short inlet and outlet conduits, where the conduit length is of the same order of magnitude as the cross-sectional dimensions. This is also the case for the Vrhovo HEPP examined in this paper. The cross-sectional area often has a complex shape. Under these conditions, standard one-dimensional elastic water hammer models may not capture the wave transmission and reflection phenomena accurately. For such cases, the rigid water hammer model is generally recommended [11], assuming an incompressible liquid and rigid pipe walls. Using this rigid model theory, the dynamics of unsteady pipe flow are described by the one-dimensional equation of motion [3]:

$$\frac{1}{\rho g}\frac{\partial p}{\partial x}+\frac{fQ|Q|}{2gDA^2}+\frac{1}{gA}\frac{dQ}{dt}=0 \tag{1}$$

in which p = pressure, ρ = liquid density, g = gravitational acceleration, f = the Darcy-Weisbach friction factor, x = distance, Q = discharge, D = conduit diameter, t = time, and A = cross-sectional area. The symbols are defined as they first appear in the paper. Equation (1) is solved together with the dynamic equation of the unit rotating masses considering the turbine performance characteristics [11]:

$$T_x = I\frac{d\omega}{dt} \tag{2}$$

in which T_x = the turbine net torque, ω = angular velocity, and I = the polar moment of inertia. The one-dimensional equation of motion for an unsteady conduit flow (Eq. (1)) can be solved either separately or simultaneously with the dynamic torque equation (Eq. (2)). Đorđević [10] developed approximate solutions of Eqs. (1) and (2) applied to the turbine emergency shutdown case separately as follows:

(i) The maximum transient pressure due to the linear single-stage closure of the turbine:

$$p_{max}=\left(1+\frac{2\sigma}{2-\sigma}\right)p_0+\rho g\Delta z+\Delta p_{loss} \tag{3}$$

in which σ = the water hammer coefficient, Δz = the elevation difference between the tailwater and datum level, Δp_{loss} = the conduit pressure losses. The water hammer coefficient is calculated by the following equation:

$$\sigma=\frac{\rho g}{p_0}\cdot G=\frac{\rho g}{p_0}\cdot\sum\frac{L_i}{A_i} \tag{4}$$

in which G = a geometric characteristic and L = the length of the conduit.

(ii) The maximum transient rotational speed after the turbine shutdown:

$$n_{max} = n_0 \cdot \sqrt{1 + \frac{364 \cdot P_0 \cdot T_f{}' \cdot f_d}{mD^2 \cdot n_0{}^2}} \tag{5}$$

in which P_0 = the initial power [kW], $T_f' = 0.65 \cdot T_f$ = the modified linear closure time T_f [s], $f_d = 1+1.25 \cdot \sigma$ = the fluid dynamic coefficient, mD^2 = the total inertia of the turbine unit`s rotating parts [tm^2], n_0 = the initial speed of rotation [min^{-1}]. Equations (3) and (4) determine the maximum pressure and turbine rotational speed in a simple waterway, respectively. However, in most engineering studies we are interested in analysing the complete dynamic evolution of pressure and rotational speed variations throughout the water hammer event. This is important, because the superposition of pressure waves in complex systems can have a significant impact on the safety of the entire hydroelectric power system. Therefore, water hammer phenomena in hydroelectric power plants should be calculated using the time-dependent method [4].

Krivchenko et al. [11] developed a numerical method for simultaneous solution of Eqs. (1) and (2). The two equations are solved simultaneously with the aid of a fourth order Runge-Kutta numerical method. The numerical algorithm can be coded in one of the computer languages or mathematical simulation packages (Fortran code in our case). Time-dependent turbine behaviour is represented using laboratory-measured turbine characteristics. Naturally, some differences exist between the steady-state and unsteady performance curves, due primarily to unsteady flow effects in the turbine flow-passage domain and when cavitation occurs.

One-dimensional water hammer models are limited in their ability to capture certain high-frequency effects in conduits or hydraulic turbines, such as draft tube vortices and rotor–stator interactions [14]. Although the 1D model is used traditionally for water hammer analysis in HEPPs, its accuracy can be improved by incorporating terms that account for multidimensional effects [15]. In contrast, three-dimensional models enable the prediction of flow variables at any location within the computational domain. However, 3D unsteady flow models are computationally demanding, and defining the right boundary conditions in hydropower structures can be challenging. While certain approximations in 3D water hammer modelling [16] may have a negligible impact in some cases, they can lead to significant systematic errors in others. Bergant and Kolšek presented a novel 3D model that is based on rigid water hammer principles tailored to bulb turbine hydropower schemes [12], [13].

The 3D model is based on the solution of the Reynolds averaged Navier-Stokes (RANS) equations coupled with the dynamic equation of the turbine unit rotating masses – Eq. (2). This method does not require a set of turbine performance characteristics data as in the 1D model. An incompressible liquid and rigid pipe walls are assumed in the model. The incompressible turbulent flow is described by the continuity equation and the Navier-Stokes equation. The Reynolds averaging yields the following two equations [17]:

$$\frac{\partial}{\partial t}\int_V \rho dV + \int_S \rho(\mathbf{v}-\mathbf{v}_S)\mathbf{n}dS = 0 \tag{6}$$

$$\frac{\partial}{\partial t}\int_V \rho\mathbf{v}dV + \int_S \rho\mathbf{v}(\mathbf{v}-\mathbf{v}_S)\mathbf{n}dS = \int_S(\boldsymbol{\tau} - \rho\overline{\mathbf{v}'\mathbf{v}'})\boldsymbol{n}dS + \int_V \mathbf{f}_b dV \tag{7}$$

in which V = volume, $\mathbf{v}$ = the flow velocity vector, $\mathbf{v}_s$ = the surface velocity vector, $\mathbf{n}$ = the unit vector, S = the surface, $\boldsymbol{\tau}$ = the stress tensor, $\rho\overline{\boldsymbol{v}'\boldsymbol{v}'}$ = the Reynolds stresses, and $\mathbf{f}_b$ = the vector of a body force per unit volume. The Reynolds stresses are calculated by the standard k-ε turbulence model [17]. Because the turbine CFD calculations involve a moving grid, the equation of space conservation must be satisfied as well:

$$\frac{\partial}{\partial t}\int_V dV + \int_S \rho\mathbf{v}_S\mathbf{n}dS = 0 \tag{8}$$

A computational domain is comprised of the whole turbine flow-passage system. A numerical finite volume method (FVM) is employed to approximate the RANS partial differential equations with algebraic ones. Bergant and Kolšek`s simulations [12], [13] used the CFD solver code ICCM COMET [18]. Their results will be used in this paper for comparison analysis.

3 Comparison between the computed and experimental results for a turbine shutdown case in the Vrhovo HEPP

Field test measurements are essential to validate an approximate model, and numerical 1D and 3D time dependent simulations. Validation of the approximate and numerical 1D water hammer models is performed traditionally by practising engineers, whereas 3D models remain the focus of active research in both industry and academia. In this study the computational results are validated against the measured results obtained in Vrhovo HEPP, Slovenia. The differences between the computed and measured results are examined for the case of an emergency shutdown of the turbine unit [12], [13].

3.1 Description of the Vrhovo HEPP

Vrhovo HEPP is the first power plant that was built in a planned chain of six run-off river type power plants on the Sava River in the south-east part of Slovenia in 1993. Vrhovo HEPP is comprised of the powerhouse and spillway structure. A vertical-slot entrance to the spawning area has been built on the right-hand-side riverbank (from the perspective of the flow direction) [19].

There are three bulb turbine units in Vrhovo HEPP, each of rated power $P_r = 11.0$ MW at the gross head $H_g = 7.5$ m. The turbine steady-state rotational speed is $n_0 = 107.14$ min^{-1} and the polar moment of inertia of the turbine unit rotating parts, including the added water mass [11], is $mD^2 = 954.6 \times 10^3$ kgm^2. The turbine flow-passage system of the Vrhovo HEPP is comprised of an upper basin, a turbine inlet conduit, a horizontal-axis double-regulated bulb turbine, an outlet conduit and a tailrace - see Fig. 1. The dimensions of the inlet and outlet conduits used in the approximate method, and the one-dimensional rigid water hammer model, are expressed as the geometrical characteristics $G_u = 0.288$ m^{-1} and $G_d = 0.557$ m^{-1}, respectively (G_u only in the approximate model). The three-dimensional water hammer model considers dimensions in the actual 3D space. Water hammer in the power plant is controlled by adjusting the guide vane and runner blade closing/opening laws properly.

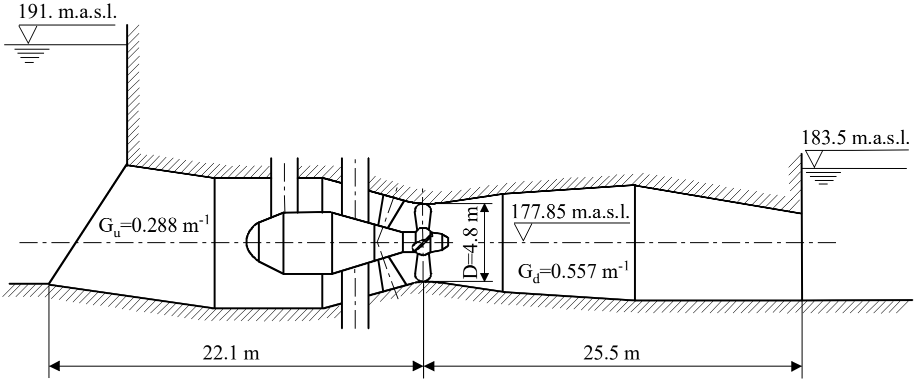

Figure 1: Layout of the Vrhovo HEPP bulb turbine flow-passage system
Source: own – adapted from [12, 13].

Field tests were performed to assess the adequacy of the designed guide vane and runner blade opening and closing laws for several water hammer scenarios, including the emergency shutdown of the turbine unit. During normal transient operating regimes, the focus lies on the two most important guaranteed parameters: (i) the maximum pressure at the turbine inlet together with the minimum pressure at the turbine outlet, and (ii) the maximum increase in the turbine unit rotational speed. These criteria were originally specified in IEC 60545:1976 [20] and most recently by IEC TS 63111:2025 [6]. Due to safety precautions, IEC 62006:2010 [21] recommends that the emergency shutdown tests should be carried out first during the commissioning of the turbine units. The results of field tests in Vrhovo HEPP showed that, for all normal operating transient regimes, the measured extreme values remained within the prescribed limits.

Continuous measurements of the guide vane and runner blade servomotor strokes y_{gv} and y_{rb}, respectively (U_x = ±0.3 %), the turbine unit rotational speed n (U_x = ±0.1 %), the pressure at the draft tube inlet p_{dt} (U_x = ±0.3 %), and the upper and lower basin water levels z_u and z_d, respectively (U_x = ±0.3 %) were carried out during an emergency shutdown of the turbine unit - see Fig. 2. The pressure in the vaneless space between the guide vanes and the runner blades, and the axial hydraulic force were measured as well, but are not considered in this paper – for details please see [12], [13]. The pressure at the turbine inlet conduit p_{ti} could not be measured due to unavailable access during the test. The uncertainty in the measurement U_x is expressed as a root-sum-square combination of the bias and precision errors [22].

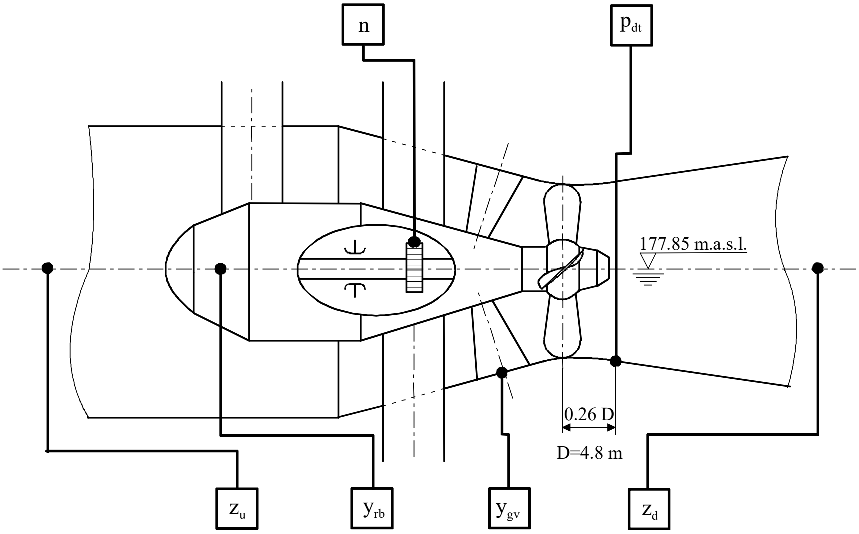

Figure 2: Position of the considered sensors for continuously measured quantities

Source: own – adapted from [12, 13].

3.2 Emergency shutdown of the bulb turbine in Vrhovo HEPP

The results are presented of an emergency shutdown of the turbine unit from the load of 10.2 MW. Initially, the electromagnetic torque of the generator drops to zero instantaneously. The guide vanes close gradually to their fully closed position, whereas the runner blades open to their fully open position. This is the most severe normal operating regime with respect to extreme transient loads at on-cam initial flow conditions.

Figure 3 shows the measured guide vane and the runner blade servomotor strokes for the considered case. A two-stroke guide vane servomotor stroke closing time function (adding a cushioning stroke) (Fig. 3a) and linear runner blade servomotor opening time function (Fig. 3b), improve the safe operation of the plant significantly (lower the maximum rotational speed rise and attenuate the pressure induced forces on the runner). The actual measured servomotor stroke was used as the input data for the numerical 1D and 3D simulations. A linear closure time T_f = 6.0 s was considered for the approximate calculations.

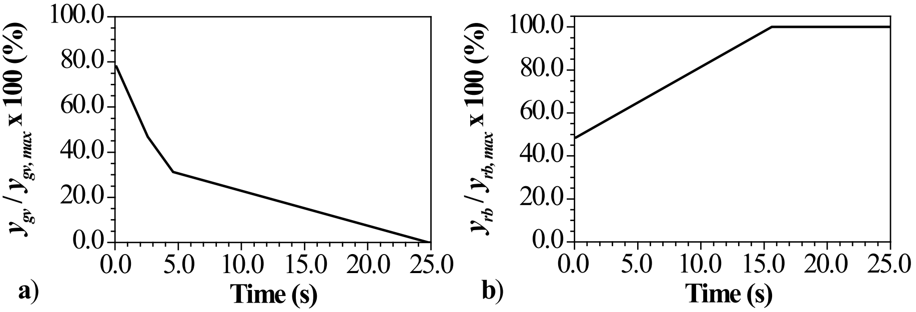

Figure 3: Guide vane (y_{gv}) and runner blade (y_{rb}) servomotor strokes

Source: own – adapted from [12, 13].

Figure 4 presents the variation of the turbine rotational speed during shutdown of the unit, which is an important regulation parameter. The agreement between the computed 1D- and 3D-model results, and the measured maximum speed rises of 48.9% and 49.4%, and 45.9%, respectively is reasonable (n_0 = 107.14 min^{-1}). The speed rise of 54.4% obtained by the approximate Eq. (5) is slightly higher than the two simulated values. Equation (5) does not consider the effect of the runner blade opening, which attenuates the maximum rotational speed rise. The computational and measured results are well within the originally proposed allowable speed rise of 75%.

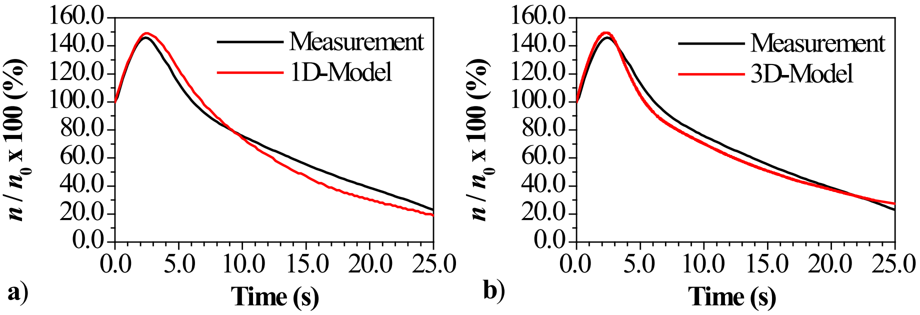

Figure 4: Computed and measured turbine rotational speed (n_0 = 107.14 min^{-1})

Source: own – adapted from [12, 13].

As stated in Section 3.1, pressure at the turbine inlet could not be measured due to unavailable access during the considered test. However, the pressure rise at the turbine inlet is an important design parameter in hydroelectric power plants with long penstocks (large water mass inertia). Figure 5 presents the turbine inlet pressure history for the 1D and 3D numerical simulations. In the case of the unit shutdown there is a maximum pressure rise of 5 % and 4 % predicted by the 1D- and 3D-models, respectively. The pressure rise predicted by Eq. (3) was 5.4%. The results calculated by the three methods are in close agreement. Finally, the maximum pressures at the datum level $z = 177.85$ m.a.s.l. obtained by the approximate, 1D and 3D numerical methods of 137 kPa, 136.5 kPa and 135.2 kPa, respectively, are less than the maximum allowable pressure of 169. kPa.

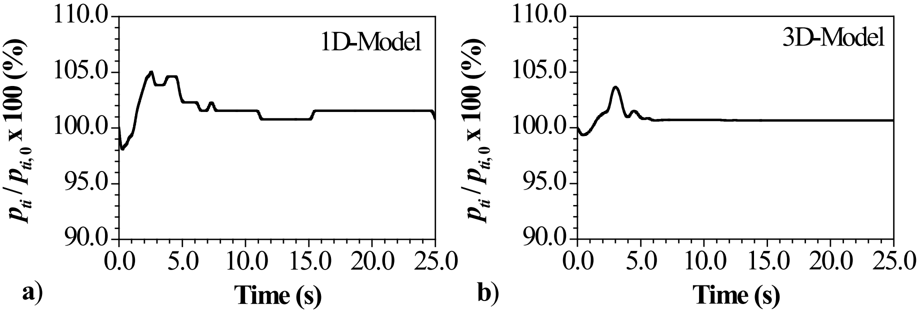

Figure 5: Computed turbine inlet conduit pressure ($p_{ti,0}$ = 130 kPa, datum level z = 177.85 m.a.s.l.)

Source: own – adapted from [12, 13].

Figure 6 compares the 1D and 3D numerically predicted and measured pressures in the draft tube inlet of the turbine (see Fig. 2). The draft tube pressure was measured at a distance of 1.25 m downstream from the runner vertical axis. The measured draft tube pressure exhibits water hammer low frequency pressure superimposed by high frequency pressure peaks that can be attributed to complex local flow behaviour in the draft tube inlet during the closure period. The minimum measured peak pressure of -25 kPa is well above the liquid vapour pressure of -100 kPa. The 1D-model predicted an average pressure at the draft tube inlet cross-sectional area at 2.02 m downstream from the runner vertical axis. The agreement of the average pressures is reasonable (Fig. 6a). However, the 1D numerical model was unable to reproduce the multidimensional and multiphase flow phenomena occurring at the draft tube inlet accurately. The 3D-model captured single-phase unsteady flow effects in the runner space, and the agreement between the computed pressure and the measured pressure was better (Fig. 6b). These two pressures are compared at the same position. The discrepancies between the 3D and measured results are due to cavitational effects. This topic is a subject of the authors' further research. However, the minimum measured and computed pressures are well above the liquid vapour pressure head of -100 kPa (no danger of water column separation). Finally, there is no reliable approximate formula for the computation of the minimum draft tube pressure due to the complex flow field at the draft tube inlet, as discussed in our case study.

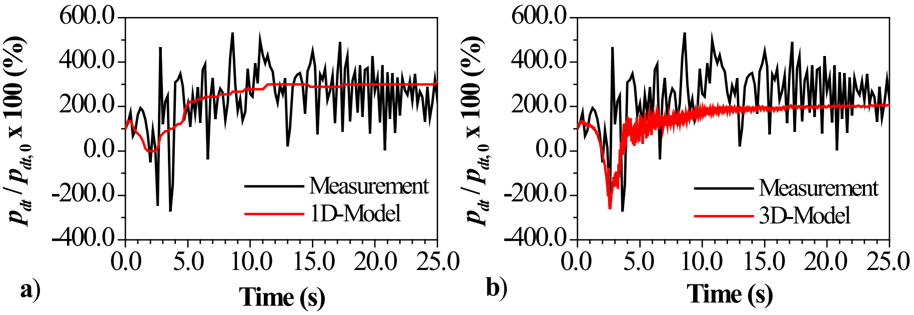

Figure 6: Computed and measured draft tube pressure ($p_{dt,0}$ = 9 kPa, datum level z = 177.85 m.a.s.l.)

Source: own – adapted from [12, 13].

4 Conclusions

The paper analyses methods for calculating hydraulic transients in hydroelectric power plants and measures for mitigation of transients. It introduces and describes the operation of the Vrhovo HEPP, which is part of the chain of hydropower plants on the lower Sava River in Slovenia. The main objective was to validate three different calculation methods for predicting transient parameters during an emergency shutdown of the bulb turbine against the site measured results. The first conclusion from the comparison of calculation and measurement results is that the extreme values of the critical transient parameters for the selected load case (emergency shutdown from 92% load) are acceptable. The maximum rotational speed rise is always below the allowed rise of 75%, the maximum turbine inlet pressure rise is always below 6%, and the minimum draft tube pressure is always well above −100 kPa. This confirms that the selected two-stroke linear closing law of the guide vane and the linear opening law of the runner blade servomotors are acceptable for the presented load case.

The calculated maximum turbine inlet pressure rise obtained using the approximate, and 1D and 3D numerical rigid water hammer models agreed well, and are 5.4%, 5% and 4%, respectively.

The calculated maximum speed rise predicted by the 1D and 3D numerical models is 48.9% and 49.4%, respectively. These results are in close agreement, whereas the approximate method (Eq. 5) predicted a higher value of 54.4%. The difference is due mainly to the influence of the runner blade opening, which attenuates the rise in rotational speed. The measured peak speed rise was 45,9%, which is slightly lower than the values predicted by the calculation methods.

Larger discrepancies were observed in the calculated values of the draft tube inlet pressure. The 1D numerical model cannot represent the multidimensional multiphase flow effects at the draft tube inlet adequately, whereas the 3D method captured single-phase unsteady flow effects downstream from the runner and predicted considerably lower minimum pressure during the emergency shutdown, which matches the measured value better. The results from the approximate method are not available, as no reliable approximate formula exists for computing the minimum draft tube pressure because of the complex flow field at the draft tube inlet, as demonstrated in this case study.

Acknowledgment

The first author acknowledges the support of the Slovenian Research and Innovation Agency (ARIS) conducted through the programme P2-0162 gratefully.

References

[1] E. Vagnoni, D. Gezer, I. Anagnostopoulos, G. Cavazzini, E. Doujak, M. Hočevar, P. Rudolf: *The new role of sustainable hydropower in flexible energy systems and its technical evolution through innovation*, Renewable Energy, Vol. 230, Paper 120832, 2024

[2] A. Bergant, J. Mazij, J. Pekolj: *Theoretical and experimental investigations of a water hammer in Sava River Kaplan turbine hydropower plants,* Journal of Energy Technology, Vol. 17, Iss. 4, p.p. 11 - 20, 2024
[3] M.H. Chaudhry: *Applied Hydraulic Transients*, Springer, 2014
[4] A. Bergant, J. Mazij, J. Pekolj, K. Urbanowicz: *Issues related to water hammer in Francis-turbine hydropower schemes: A review*, Energies, Vol. 18, Paper 6404, 2025
[5] S. Pejović, A.P. Boldy, D. Obradović: *Guidelines to Hydraulic Transient Analysis*, Gower Technical Press Ltd., 1987
[6] IEC TS 63111: *Hydraulic Turbines, Storage Pumps and Pump-Turbines – Hydraulic Transient Analysis, Design Considerations and Testing*, International Electrotechnical Commission, 2025
[7] E. B. Wylie, V. L. Streeter: *Fluid Transients in Systems*, Prentice Hall, 1993
[8] J. Fašalek, S. Rakčević: *Air valves and control of the Kaplan turbine during transients,* 13th IAHR Symposium on Hydraulic Machinery and Cavitation, Montréal, 1986
[9] J.H. Gummer: *Predicting draft tube water column separation in Kaplan turbine,* The International Journal of Hydropower & Dams, Vol. 10, Iss. 3, p.p. 80 - 83, 2003
[10] B. Đorđević: *Korišćenje Vodnih Snaga. Objekti Hidroelektrana (Use of Water Power. Hydraulic Power Plant Facilities),* Građevinski fakultet and Naučna knjiga, 1984 (in Serbian)
[11] G.I. Krivčenko, N.N. Aršenevski, E.V. Kvjatovskaja, V.M. Klabukov: *Gidromehaničeskie Perehodnie Processi v Gidroenergetičeskih Ustanovkah (Hydromechanical Transient Regimes in Hydroelectric Power Plants)*, Energija, 1975 (in Russian)
[12] A. Bergant, T. Kolšek: *Developments in bulb turbine three-dimensional water hammer modelling,* 21st IAHR Symposium on Hydraulic Machinery and Cavitation, Lausanne, 2002
[13] A. Bergant, T. Kolšek: *Comparison of one- and three-dimensional models for water hammer analysis in bulb turbine hydropower plants,* 9th International Conference on Pressure Surges, Chester, 2004
[14] S. Salehi, H. Nilsson, E. Lillberg, N. Edh: *An in-depth numerical analysis of transient flow field in a Francis turbine during shutdown,* Renewable Energy, Vol. 179, p.p. 2322 - 2347, 2021
[15] A. Bergant, Z. Rek, K. Urbanowicz: *Numerical 1D and 3D water hammer investigations in a simple pipeline apparatus,* Strojniški vestnik – Journal of Mechanical Engineering, Vol. 71, Iss. 5-6, p.p. 149 - 156, 2025
[16] C. Trivedi, O.G. Dahlhaug: *A comprehensive review of verification and validation techniques applied to hydraulic turbines,* International Journal of Fluid Machinery and Systems, Vol. 12, Iss. 4, p.p. 345 - 367, 2019
[17] J.H. Ferziger, M. Perić: *Computational Methods for Fluid Dynamics*, Springer-Verlag, 1999
[18] ICCM GmbH: *Comet Version 2.00. User Manual*, Institute of Computational Mechanics, 2000
[19] G. Kolman, M. Mikoš, M. Povž: *Ribji prehodi na hidroenergetskih pregradah v Sloveniji (Fish passages on hydroelectric power dams in Slovenia),* Varstvo narave, Vol. 24, p.p. 85 - 96, 2010 (in Slovene)
[20] IEC 60545: *Guide for Commissioning, Operation and Maintenance of Hydraulic Turbines*, International Electrotechnical Commission, 1976
[21] IEC 62006: *Hydraulic Machines—Acceptance Tests of Small Hydroelectric Installations*, International Electrotechnical Commission, 2010
[22] H.W. Coleman, W.G. Steele: *Experimentation and Uncertainty Analysis for Engineers*, John Wiley and Sons, 1989

Povzetek v slovenskem jeziku

Približne, numerične in eksperimentalne raziskave vodnega udara v hidroelektrarni s cevnimi turbinami Vrhovo. V prispevku raziskujemo učinkovitost in natančnost približnih in numeričnih modelov vodnega udara v slovenskih hidroelektrarnah s cevnimi turbinami na reki Savi. Najprej so predstavljeni približni in numerični modeli togega vodnega udara. Rezultati izračuna so primerjani z rezultati meritev v hidroelektrarni Vrhovo. Izračunane in izmerjene vrednosti so primerjane za obratovalni režim nujne hitre zapore turbine. Vodni udar krmilimo z ustrezno nastavitvijo zakonov zapiranja/odpiranja lopatic vodilnika in gonilnika. Med približnimi in numeričnimi, in izmerjenimi rezultati obstaja dobro ujemanje.

JOURNAL OF ENERGY TECHNOLOGY
Vol. 18, No. 4, pp. 203–212, December 2025

Original
Scientific
Article

Submitted
24. 11. 2025

Accepted
27. 11. 2025

Published
31. 12. 2025

MEASUREMENT-BASED EVALUATION OF DISTRIBUTION TRANSFORMER LOSSES CHARACTERISTICS FOR SUSTAINABLE VOLTAGE REGULATION

LIDIJA M. KORUNOVIĆ
University of Niš, Faculty of Electronic Engineering, Niš, Serbia
lidija.korunovic@elfak.ni.ac.rs

CORRESPONDING AUTHOR
lidija.korunovic@elfak.ni.ac.rs

Abstract This paper presents the characteristics of distribution transformer losses obtained on the basis of field measurements in a distribution grid. The active and reactive powers were recorded simultaneously at both 110 kV and 35 kV transformer voltage levels in different periods of the days, when the position of the on-load tap changer was changed intentionally. The variations of total transformer losses during these experiments were modelled by exponential models. The parameters of the models were grouped according to the particular daily periods, analysed statistically and compared with corresponding parameters of transformer load models. The importance was emphasised of knowing transformer losses characteristics in the networks with a significant share of distributed generation, energy storage systems and electric vehicles.

Keywords
distribution transformer,
measurements,
losses,
characteristics,
sustainability,
voltage regulation

https://doi.org/10.18690/jet.18.4.203-212.2025

University of Maribor Press

1 Introduction

Today, a large number of new load devices are used, and there is a need to determine both their characteristics and the characteristics of the aggregate load in which they participate [1]. In addition, there is a global trend of liberalisation of the electricity market, in which electricity becomes a commodity like any other. Under these circumstances, it is extremely important to know the precise consumption data, including data on which load model is adequate and the values of its parameters. These data are included as input data in various steady state and dynamic analyses of power grids and systems, and can be used both in their operation and planning [2]. The accuracy of the calculation results depends strongly on the accuracy of the input data, as stated in many references, such as [3].

In addition to the massive use of new load devices, modern power grids are characterised by the increasing use of distributed energy sources, energy storage systems and electric vehicles, which introduces new components to be modelled. For example, electric vehicles (EVs) in battery charging mode represent a load, but they can also be used as sources of electricity [4]. The unpredictability of electricity production from renewable energy sources (RESs) and the consumption/production of EVs, can lead to numerous problems in the operation of the electricity grid. Therefore, it is necessary to improve the control and protection of the grid, which, along with the infrastructure advances, lead to the emergence of smart grids [5]. One of the very important issues in the modern power grids is maintaining stable voltage levels, often called the sustainable voltage regulation. It ensures grid reliability, prevents equipment damage by managing the fluctuations caused by variable generation and demand, and improves energy efficiency, which represents one of the pillars of the sustainable energy transition [6].

For sustainable voltage regulation, the load-to-voltage characteristics of aggregate loads connected to the network buses are very important. These can be obtained by the measurement-based approach and the aggregation-based approach. The former is recommended, because the aggregation-based approach requires data on the model parameters of all load devices, as well as data on the aggregate load structure, which is very difficult to know precisely. The measurement-based approach implies field measurements carried out either during the experiments in an electric power system, or during the continuous system operation [7].

This paper is the continuation of the research [8], that deals with identification of the statistically reliable parameters of load-to-voltage characteristics of an aggregate load on the basis of experiments in a distribution network. Given that accurate models of transformers (and lines) are also important for network analysis, this paper deals with the modelling of distribution network transformer losses in terms of their dynamic responses to voltage changes.

2 Description of Measurements

Simultaneous measurements of the voltage and active and reactive powers were performed at the 35 kV and 110 kV levels of a 31.5 MVA transformer in the transformer substation TS "Niš 13", in the winter season. Two three-phase power analysers [9] were connected via the existing voltage and current transformers. Experiments of on-load tap changes were carried out on two weekdays in different periods of time: morning, afternoon and night, while each series of experiments consisted of 5 to 9 voltage changes, providing enough data for statistically reliable parameters of the transformer losses models. During the experiments, the average voltage, active and reactive power values were recorded by the analyser, each second.

The power losses of the transformer were obtained as the difference of the measured powers on its primary and secondary sides. They were analysed, and subsequently modelled with adequate models. In all the considered operating regimes, the active power losses ranged from approximately 0.112 MW to 0.163 MW, and were of the order of magnitude of the percentage of active power measured at the transformer primary. The reactive power losses were significantly higher, and ranged from 0.841 Mvar to 1.491 Mvar, which, on average, amounted to slightly more than a quarter of the reactive power recorded at the 110 kV transformer level.

3 Applied Models

Figure 1 depicts the active power losses of the transformer during two consecutive experiments of changing the transformer ratio in the (weekday) evening. The active power losses change with the voltage, but the influence of stochastic load changes are so large that the attempt to fit the measured values with the exponential dynamic model described in [10] gave very small correlation coefficients, about 0.1, for both consecutive responses. Similar values of the correlation coefficient were obtained for other responses of active power losses. Taking into account the variations of active power losses even when the voltage was almost constant, the average values of the losses were considered, and the losses were modelled with the exponential static model in the form:

$$\Delta P = \Delta P_0 \left(\frac{U}{U_0} \right)^{\alpha_s}, \qquad (1)$$

where: ΔP and ΔP_0 represent the average values of the active power losses after and before the voltage change, respectively; U and U_0 are the average voltage values at a 35 kV voltage level after and before the voltage change; and α_s is a steady state voltage exponent of the active power losses. This exponent is denoted commonly as k_{pu} in an exponential static load model [7]. From the two experimental data in Figure 1, α_s =1.03 and α_s =0.73 were obtained, respectively.

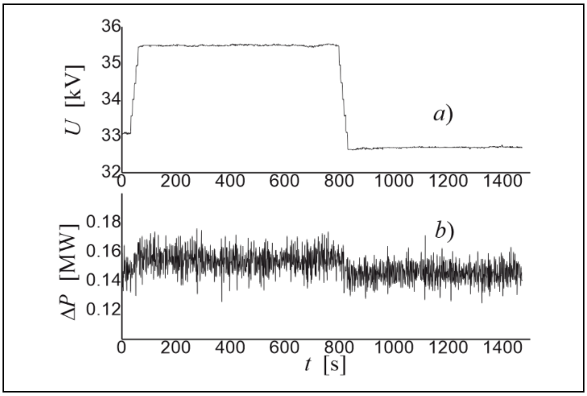

Figure 1: Voltage at the 35kV level a), and transformer active power losses b) during two consecutive experiments

The analysis of reactive power losses showed that the losses change simultaneously with the voltage and recover after these changes. It was found that reactive power losses can be modelled by an exponential dynamic model during all the examined voltage changes, with a correlation coefficient greater than, or equal to 0.7. For illustration, Figure 2 depicts: the voltage changes on the secondary side of the transformer during the experiments from Figure 1, and the corresponding responses of the reactive power losses to these changes. The same Figure also presents the fitted curves in the form:

$$\Delta Q(t)=\left(\Delta Q_0\left(\frac{U}{U_0}\right)^{\beta_s}-\Delta Q_0\left(\frac{U}{U_0}\right)^{\beta_t}\right)\cdot\left(1-e^{-t/T_q}\right)+\Delta Q_0\left(\frac{U}{U_0}\right)^{\beta_t} . \tag{2}$$

In (2), the previously not mentioned variables and parameters are: $\Delta Q(t)$ and ΔQ_0 – reactive power losses in the time domain during the experiment, and the initial value of the reactive power losses before the voltage change, respectively; T_q – the recovery time constants of the reactive power losses, β_s – the steady state voltage exponent of the reactive power losses, β_t – the transient voltage exponents of the reactive power losses. The identified parameters of model (2) on the basis of two consequent experiments, are: $\beta_s=0.53$, $\beta_t=1.17$ and $T_q=143.7$ s; and $\beta_s=0.71$, $\beta_t=1.26$ and $T_q=54.9$ s, respectively.

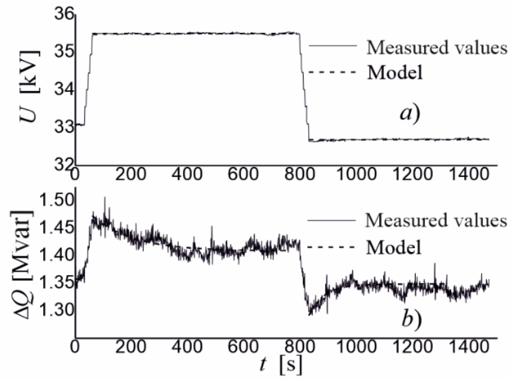

Figure 2: Voltage at the 35kV level a), and reactive power losses of the transformer b), during two consecutive experiments, together with the corresponding model

4 Characteristics of Active and Reactive Power Losses

Models (1) and (2) were used for modelling of active and reactive power losses, respectively, during all the performed experiments of voltage changing on two weekdays, in the morning, afternoon and evening. It was found that they depend on the operating regime of the transformer. A statistical analysis of the identified α_s values yielded the following average values: 0.59, 0.20 and 0.94, in the morning, afternoon and evening, respectively. Regardless of these differences, a general conclusion can be drawn that this parameter active power losses is smaller than the corresponding α_s parameter of total transformer load at the 35 kV level, in the same (winter) season. These parameters are: 1.20 in the morning, 1.19 in the afternoon and 1.25 in the evening [8]. However, the influence of active power losses characteristics on the behaviour of the total load at the 110 kV level can be neglected, since, as mentioned, the transformer active power losses are very small in comparison with the active power at the 110 kV level. In general, the characteristics of active power losses have a minor influence on the load-to-voltage characteristics of the load at higher voltage levels, and, consequently, will have almost no effect on the future grids with significant generation from RESs, with energy storage systems (ESSs), as well as numerous EVs connected to the network and operating as consumers/sources of energy.

Table 1: Parameters of the exponential dynamic model of: reactive power losses and reactive transformer load at 35 kV and 110 kV, in different daily periods during the winter season

	Morning	Afternoon	Evening
β_s	0.71	0.64	0.78
β_{s_35}	4.43	4.99	4.16
β_{s_110}	3.49	3.87	3.15
β_t	1.38	1.26	1.31
β_{t_35}	4.79	5.30	4.62
β_{t_110}	3.93	4.29	3.62
T_q [s]	172.8	134.9	134.2
T_{q_35} [s]	136.8	117.7	80.2
T_{q_110} [s]	133.5	124.7	89.6

Table 1 lists the average values of the exponential dynamic model of reactive power losses – β_s, β_t, and T_q, identified in different daily periods: morning, afternoon and evening. For comparison, the parameters of the total reactive load of the transformer at the 35 kV level, β_{s_35}, β_{t_35}, and T_{q_35}, and these parameters of the total reactive load at the 110 kV level (β_{s_110}, β_{t_110} and T_{q_110}), all obtained in the winter season, are also presented in Table 1.

It can be noted that the values of β_s , and β_t that characterise the reactive power losses, are much smaller than the corresponding values of the parameters of the reactive transformer load at the 35kV level. Thus, the characteristics of reactive power losses result in smaller values of β_{s_110} and β_{t_110} in comparison with β_{s_35} and β_{t_35}. Similarly, larger values of the recovery time constants of reactive power losses than the time constants of a reactive load at a 35 kV voltage level, cause the decrease of recovery time constant at the 110 kV level. Therefore, the characteristics of transformer reactive power losses should be included in both static and dynamic analysis of electric power networks. They influence the load-to voltage characteristics of the transformer load at its primary, and, therefore, the obtained characteristics of transformer reactive power losses should be included in the voltage regulation problem.

5 Conclusion

The analysis of the variations of total transformer losses during the experiments of transformer ratio changes showed that the active and reactive power losses can be modelled by exponential static and an exponential dynamic model, respectively. The parameters of the model of active power losses were obtained and analysed in different daily periods. It was pointed out that they do not affect the characteristics of active power load of the transformer significantly. On the other hand, the characteristics of reactive power losses decrease both steady state and transient voltage exponents notably, and recovery time constant, of total reactive load at the transformer primary. Therefore, the dynamic characteristics of reactive power losses of distribution transformers should play an important role in modelling aggregate distribution loads for different purposes, including sustainable voltage regulation in networks with RESs, ESSs and EVs.

Acknowledgment

This work was supported by TRANSIT: Transition to Sustainable Future through Training and Education project under EU Horizon Grant No. 101075747 and by the Ministry of Science, Technological Development and Innovation of the Republic of Serbia [Grant Number: 451-03-136/2025-03/200102].

References

[1] Korunović, L. M., Milanović, J. V., Djokic, S. Z., Yamashita, K., Villanueva, S. M., Sterpu, S. (2018). Recommended Parameter Values and Ranges of Most Frequently Used Static Load Models. *IEEE Transactions on Power Systems*, *33,* 5923-5934. DOI: 10.1109/TPWRS.2018.2834725

[2] Milanović, J. V., Yamashita, K., Villanueva, S. M., Djokic, S. Ž., Korunovic, L. M. (2013). International Industry Practice on Power System Load Modeling. *IEEE Transactions on Power Systems*, *28,* 3038-3046. DOI: 10.1109/TPWRS.2012.2231969

[3] Nitsch, D., Vennegeerts, H. (2024). Evaluation of Simulations for Short-Term Voltage Stability Assessment with Respect to Model Uncertainties. *Eng, 6,* 1-20. https://doi.org/10.3390/eng6030041

[4] Veisi, M. (2025). Stochastic economic placement and sizing of electric vehicles charging station with renewable units and battery bank in smart distribution network. *Scientific Reports, 15,* 1-20. https://www.nature.com/articles/s41598-025-10391-6

[5] Powell, J., McCafferty-Leroux, A., Hilal, W., Gadsden, S. A. (2024). Smart grids: A comprehensive survey of challenges, industry applications, and future trends. *Energy Reports, 11,* 5760-5785. https://doi.org/10.1016/j.egyr.2024.05.051

[6] Licari, J., Rhaili, S. E., Alexander Micallef, A., Staines, C. S. (2025). Addressing voltage regulation challenges in low voltage distribution networks with high renewable energy and electrical vehicles: A critical review. *Energy Reports, 14*, 2977-2997. https://doi.org/10.1016/j.egyr.2025.09.030

[7] WG C4.605. (2014). Modelling and Aggregation of Loads in Flexible Power Networks, CIGRE, 566, https://www.e-cigre.org/publications/detail/566-modelling-and-aggregation-of-loads-in-flexible-power-networks.html

[8] Korunović, L.M. (2008). Modelling of Medium Voltage Distribution Network Load on the Basis of Experiments. *University of Niš, Faculty of Electronic Engineering,* 2008. (in Serbian)

[9] Chauvin Arnoux. (2025). Three Phase Power Quality Analyser C.A 8332B and C.A 8334B User's Manual. https://www.manualslib.com/manual/1181562/Chauvin-Arnoux-C-A-8334b.html

[10] Stojanović, D., Korunović, L., Milanović, J. V. (2008). Dynamic load modelling based on measurements in medium voltage distribution network, *Electric Power Systems Research, 78,* 228-238. https://doi.org/10.1016/j.epsr.2007.02.003

About the author

Lidija M. Korunović received her Dipl.Ing., MSc and PhD degrees from the Faculty of Electronic Engineering - University of Niš (UNI-FEE), Serbia. She is a full Professor at the same Faculty. From 2016 to 2023 she was the Head of the Department of Power Engineering at the UNI-FEE. The main areas of her research are load modelling, power quality and distribution systems. Lidija M. Korunović has published more than a hundred scientific papers in international and national journals and conference proceedings, two memoirs, two textbooks, two technical solutions and two technical reports, which are the results of her membership in two CIGRE/CIRED working groups. She took part in ten scientific projects and studies supported by the Serbian Ministry of Science. She is the team leader of the TRANSIT project (funded by the EU) within UNI-FEE.

Povzetek v slovenskem jeziku

Merilno podprta analiza značilnosti izgub distribucijskih transformatorjev za trajnostno regulacijo napetosti. Članek obravnava značilnosti izgub distribucijskih transformatorjev, določene na podlagi terenskih meritev v distribucijskem elektroenergetskem omrežju. Aktivna in jalova moč sta bili sočasno merjeni na transformatorskih napetostnih nivojih 110 kV in 35 kV v različnih obdobjih dneva, pri čemer je bil položaj obremenitvenega preklopnika (OLTC) namerno spreminjan. Spremembe skupnih izgub transformatorja med izvedenimi preizkusi so bile modelirane z eksponentnimi modeli. Parametri modelov so bili razvrščeni glede na posamezna dnevna obdobja, statistično analizirani ter primerjani z ustreznimi parametri modelov obremenitve transformatorja. Poudarjen je bil pomen poznavanja značilnosti izgub transformatorjev v omrežjih z velikim deležem razpršene proizvodnje, sistemov za shranjevanje energije in električnih vozil.

JOURNAL OF ENERGY TECHNOLOGY
Vol. 18, No. 4, pp. 213–230, December 2025

Original
Scientific
Article

Submitted
5. 12. 2025

Accepted
16. 12. 2025

Published
31. 12. 2025

OPERATIONAL AND THERMODYNAMIC METHODOLOGY FOR INTEGRATING A GAS–STEAM CYCLE INTO A LEGACY COAL-FIRED POWER BLOCK

DUŠAN STRUŠNIK
Energetika Ljubljana d.o.o. TE-TOL Unit, Ljubljana, Slovenija
dusan.strusnik@gmail.com

CORRESPONDING AUTHOR
dusan.strusnik@gmail.com

Abstract This paper investigates the thermodynamic integration of a gas–steam combined cycle into an existing coal-fired power block with the objective of reducing coal utilisation and associated emissions. In the baseline configuration, the legacy unit relies entirely on pulverised coal combustion, whereas the retrofit concept introduces a natural gas-fired gas turbine with heat recovery steam generation. The recovered exhaust heat is used to supplement steam production for the existing steam turbine train, thereby increasing the overall cycle efficiency and enabling partial fuel substitution. From an ecological perspective, natural gas presents a significantly lower carbon emission factor compared to coal, resulting in a proportional reduction of CO_2 and other greenhouse gas emissions at the system level. Additional benefits include lower NO_x formation due to cleaner combustion and improved operational flexibility, enabling more efficient load following under variable renewable penetration. The results suggest that such hybridisation offers a viable decarbonisation pathway for thermal assets by leveraging the existing infrastructure while achieving meaningful reductions in specific emissions.

Keywords
natural gas,
power,
recovery,
steam,
turbine

---

https://doi.org/10.18690/jet.18.4.213-230.2025

University of Maribor Press

The integration of a gas–steam combined cycle into a legacy coal-fired power block represents a transitional decarbonisation approach that combines thermodynamic efficiency gains with significant ecological benefits. In the retrofit concept, the existing coal boiler is removed fully and replaced by a gas turbine (GT), heat recovery steam generator (HRSG) that utilises the high-temperature GT exhaust gases from two independent gas–steam blocks. The original steam turbine and district heating (DH) station are retained to preserve both power production and cogeneration functionality. Each HRSG generates high-pressure (HP) steam at approximately 95 bar and 520 °C, and intermediate-pressure (IP) steam at approximately 9.5 bar and 250 °C, as well as heat for district heating [1]. The HP and IP steam streams are supplied to the existing extraction-condensing steam turbine (ST), while the turbine extractions provide IP and low-pressure steam for industrial uses and district heating. Figure 1 shows the principle of operation of the existing coal-fired boiler and the gas–steam combined cycle.

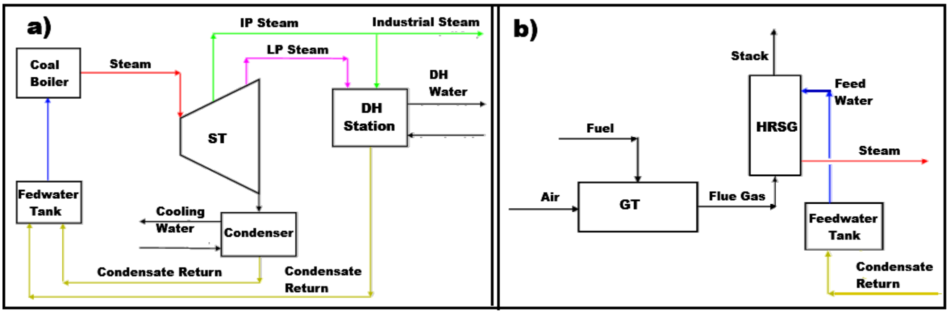

Figure 1: a) Principle of operation of: (a) the existing coal-fired boiler, and (b) the gas–steam combined cycle.

In the existing coal-fired boiler pulverised coal is combusted with air in the furnace to generate thermal energy. The released heat is transferred to the boiler heat-exchange surfaces, where the feedwater is converted into high-pressure steam. The HP steam is supplied to an ST, where a portion of the steam is extracted for DH station and industrial steam supply. The remaining steam expands further through the ST to the condenser, where it is condensed. The resulting condensate is then returned to the feedwater system. The flue gases pass through superheaters, economisers, and air preheaters before being discharged through the stack, while the ash and particulate matter are removed by appropriate gas-cleaning systems [2].

In the gas–steam combined cycle, natural gas is combusted in a GT, producing mechanical power and high-temperature exhaust gases. The exhaust heat is recovered in an HRSG, which generates HP and IP steam, as well as thermal energy for DH. The HP and IP steam are supplied to the existing steam turbine, where they expand to produce additional power. After expansion the steam is condensed, and the resulting condensate is returned to the feedwater tank via the condensate return line. By utilising the GT exhaust heat, the combined cycle increases overall plant efficiency and reduces specific fuel consumption significantly.

From an ecological perspective, the substitution of coal combustion with natural gas reduces specific CO_2 emissions and associated pollutants such as SO_2, particulates, and heavy metals significantly. Thermodynamically, the combined cycle configuration enhances exergy utilisation through heat recovery and multi-pressure steam generation, leading to increased overall efficiency and improved seasonal operation tied to the district heating demand. Collectively, the proposed hybridisation offers a viable pathway for reducing coal dependency, while extending the lifetime and functional value of the existing thermal assets. The operating principle of integrating two gas–steam combined-cycle units into the existing ST and DH system is shown in Fig. 2

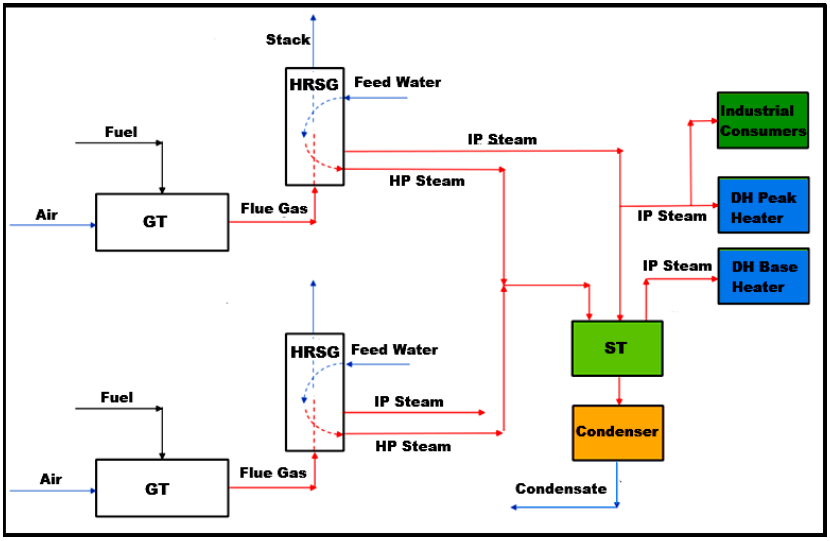

Figure 2: Operating principle of integrating two gas–steam combined-cycle units into the existing ST and DH system.

The proposed configuration consists of two independent gas–steam combined-cycle units connected to a single existing ST, which enables efficient utilisation of the existing infrastructure and reduces the overall investment costs. Each combined-cycle unit comprises a GT and an HRSG, Fig. 3. Natural gas is combusted in the GTs to generate electrical power, while the high-temperature exhaust gases are recovered in the HRSGs. The HP and IP steam generated in the HRSGs are supplied to the existing ST. The steam expands through the ST to produce additional electrical power, while controlled steam extractions are used for the DH and industrial steam supply, allowing a combined heat and power operation with high overall efficiency. The remaining steam expands to the condenser, where it is condensed, and the condensate is returned to the feedwater system.

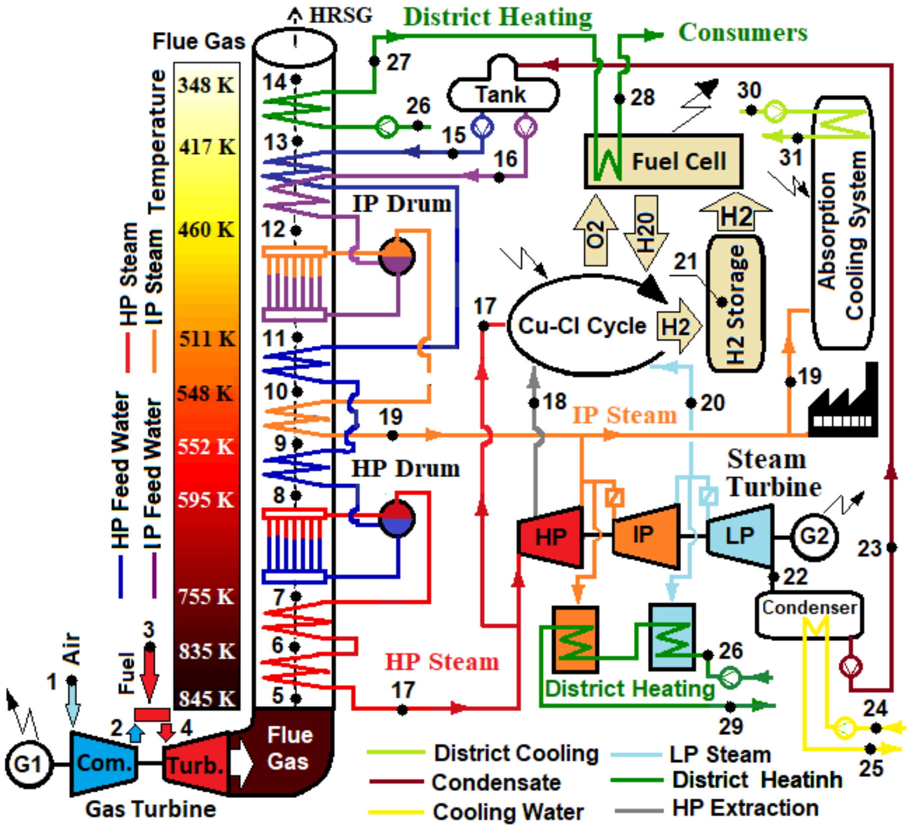

Figure 3: Configuration of independent gas–steam combined-cycle units connected to a existing ST [2].

The independent operation of the two combined-cycle units provides high operational flexibility and availability, enabling stable electricity and heat supply under varying load conditions and during maintenance or partial outages. The integration of gas–steam cycles improves fuel utilisation, reduces specific CO_2 emissions, and enhances the overall efficiency of the energy system significantly. Despite its advantages, the proposed configuration introduces increased system complexity, particularly in steam system control and coordination between multiple HRSGs and the existing ST. Variations in the steam parameters may impose operational constraints on the turbine, while the use of natural gas increases the exposure to fuel price volatility and supply risks. In addition, the capital and maintenance costs are higher compared to a single combined-cycle configuration.

Fig. 4 illustrates an existing condensing ST configuration operated within a closed Rankine cycle and equipped with a surface condenser and four steam extraction points. During steady-state operation, high-pressure superheated steam expands through the turbine's high-, intermediate-, and low-pressure stages, thereby converting the steam enthalpy into mechanical shaft work. The exhausted wet steam is directed to the surface condenser, where condensation occurs under sub-atmospheric pressure conditions [3]. By maintaining a deep vacuum, the condenser increases the overall expansion ratio and enhances the cycle's thermodynamic efficiency. Simultaneously, the condenser provides the heat sink for phase change, and enables the recovery of condensate for subsequent pressurisation by the condensate and feedwater pump train, thus ensuring closed-loop mass continuity within the water–steam circuit.

The four-turbine extraction, Fig. 4, serves distinct thermal and process functions. The first two extractions supply steam for regenerative heating of the condensate and feedwater. The regenerative preheating reduces the temperature differential across the HRSG heat exchangers, thereby decreasing the exogenous heat input requirements and improving the overall thermal efficiency of the Rankine cycle. The third extraction originates from the IP section and supports primarily process-level heat integration within the plant's balance of system. The fourth extraction originates from the LP turbine section and is utilised for district heating of the adjacent urban network, supplying low- to medium-grade thermal energy suitable for space-heating applications. The integration of district heating increases the overall plant exergy utilisation otherwise rejected thermal energy and contributes to improved seasonal utilisation factors.

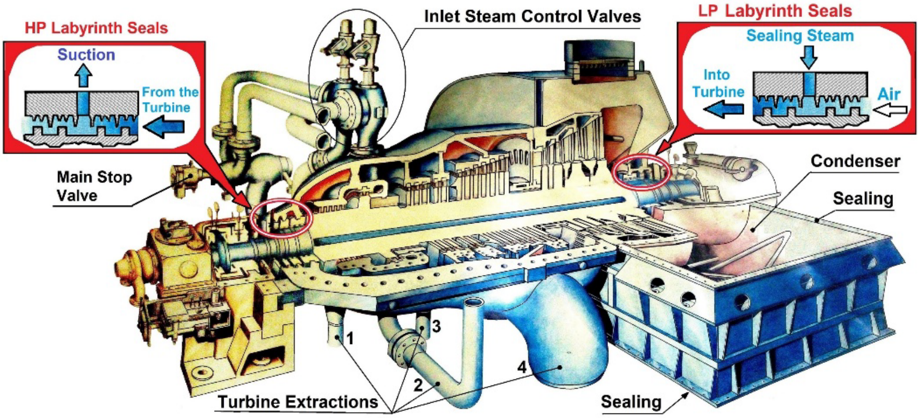

Figure 4: Existing condensing ST with condenser and four turbine extractions [4]**.**

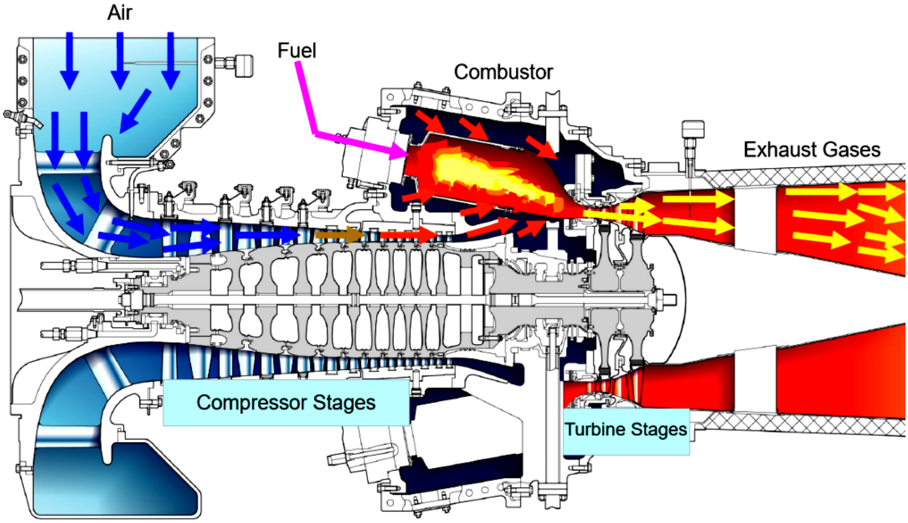

Figure 5: 5. Cross-section of the Siemens SGT-800 gas turbine [5]**.**

Fig. 5 illustrates the main components and operating principle of the Siemens SGT-800 industrial gas turbine, which is a single-shaft, high-efficiency Brayton-cycle unit intended for combined-cycle power generation, industrial cogeneration and district heating applications. The turbine integrates an axial compressor, combustor and multi-stage power turbine on a common shaft, enabling efficient conversion of chemical fuel energy into mechanical and electrical power while providing high-grade exhaust heat for downstream heat recovery in the HRSG.

Fig. 6 shows an HRSG cross-section of the layout of the HP and IP evaporator heat exchangers, the corresponding HP and IP steam drums, and the superheater bundles. Hot exhaust gases from the gas turbine pass sequentially through the heat-transfer surfaces, thereby enabling multi-pressure steam generation and superheating in the HRSG.

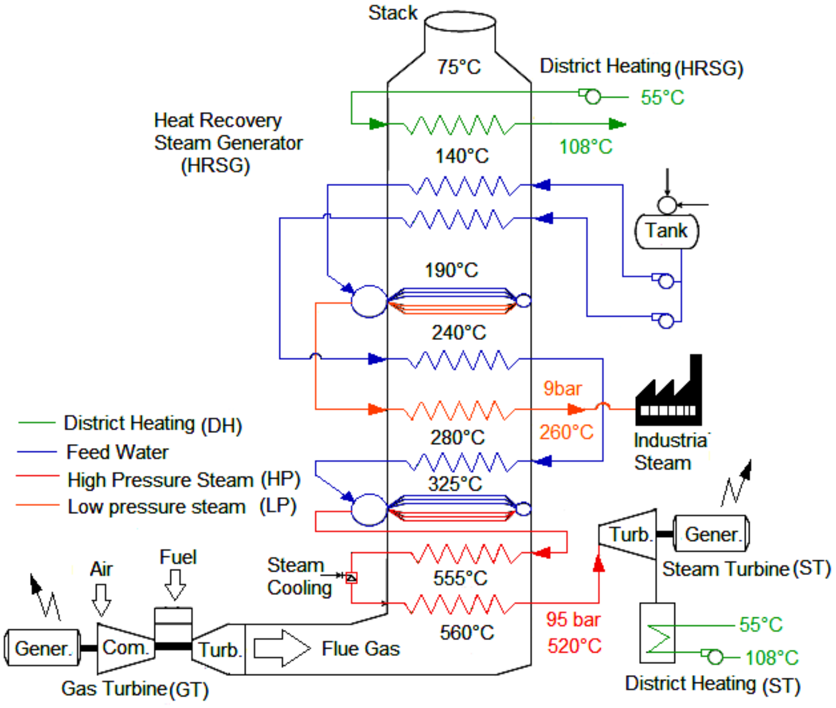

Figure 6: Cross-section of the HRSG and the flow direction of the hot GT exhaust gases [6]**.**

In the steam generation process, feedwater enters the HRSG at a pressure slightly above the final HP and IP steam pressures. Within the HP and IP evaporator sections, the water undergoes a phase change, forming a water–steam mixture which, subsequently, enters the respective HP and IP drums. In each drum, the water and steam are separated via natural circulation. The water is recirculated back to the evaporator tubes, while the dry saturated steam is directed to the HP and IP superheaters, where it is heated to the final fresh-steam temperature. The superheated HP and IP steam streams are then supplied from the HRSG to the existing ST for further expansion and power generation.

2 The thermodynamic methodology for integrating a gas–steam cycle into a legacy coal-fired power block

The proposed thermodynamic methodology for retrofitting a legacy coal-fired power block with a gas–steam combined arrangement is based on the integration of a Brayton cycle gas turbine subsystem with the existing Rankine cycle steam turbine. Such integration enables the utilisation of high-temperature heat from the gas turbine exhaust to augment the steam production and improve the overall thermal efficiency of the plant without extensive modification of the installed steam cycle infrastructure. This approach is particularly suitable for coal-fired units with a sufficient steam path margin and appropriate mechanical design allowances for elevated steam mass flows and temperatures.

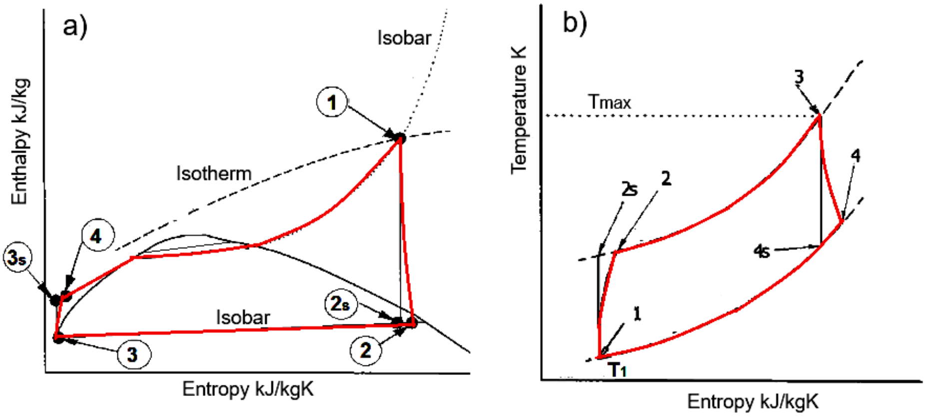

Figure 7: Thermodynamic diagrams of a) the Rankine cycle, and b) the Brayton cycle.

From a thermodynamic perspective, the combined configuration exploits the complementary characteristics of the Brayton and Rankine cycles. The Brayton cycle consists of the compression of ambient air in a gas compressor, followed by constant-pressure fuel combustion within a combustor, and subsequent expansion of the high-temperature gases in a GT. The relatively high turbine outlet temperature (typically exceeding 773–873 K) provides a viable source of thermal energy for an HRSG. A schematic representation of the thermodynamic diagrams for both the Brayton and Rankine cycles, including their principal processes and state points, is provided in Fig. 7.

The thermodynamic assessment of replacing a conventional coal-fired boiler–ST system with a gas–steam combined cycle requires explicit consideration of the energy and exergy balances, combustion thermochemistry, heat recovery and steam cycle integration. The formulations of the energy, First Law, and exergy, Second Law, balances serve as the fundamental thermodynamic framework for evaluating system performance and assessing the irreversibilities within the integrated gas–steam retrofit configuration. For the energy balance, the First Law, the steady-state formulation is [7]:

$$\dot{Q} - \dot{w} = \sum \dot{m}_i \cdot \left(h_i + \frac{v_i^2}{2} + g \cdot z_i\right)_{in} - \sum \dot{m}_e \cdot \left(h_e + \frac{v_e^2}{2} + g \cdot z_e\right)_{out} \qquad (1)$$

where $\dot{Q}_{cv}$ is the heat transfer rate, $\dot{w}$ is the work transfer rate, $\dot{m}_i$ is the inlet mass flow rate, h_i is the inlet specific enthalpy, v_i is the inlet specific velocity, g is the gravitational acceleration, z_i is the inlet elevation (potential term), $\dot{m}_e$ is the outlet mass flow rate, h_e is the outlet specific enthalpy, v_e is the outlet specific velocity, and z_e is the outlet elevation, potential term. For HRSG comparison, the kinetic and potential terms are negligible, yielding [8]:

$$\dot{Q}_{fuel} - \dot{w} = \dot{m}_{steam} \cdot (h_{out} - h_{in}) \qquad (2)$$

where $\dot{Q}_{fuel}$ is the fuel heat input, $\dot{m}_{steam}$ is the steam mass flow, h_{out} is the steam specific enthalpy from the HRSG, and h_{in} is the HRSG feedwater specific enthalpy. The Brayton cycle performance is calculated as [9]:

- Compressor work: $w_c = c_a \cdot (T_2 - T_1)$, (3)
- Turbine work: $w_t = c_f \cdot (T_3 - T_4)$ and (4)
- Net specific work: $w_{GT} = w_t - w_c$ (5)

where w_c is the specific work input to the compressor, c_a is the specific heat of air, T_2 is the compressor outlet temperature, T_1 is the compressor inlet temperature, w_t is the specific work produced by the GT, c_f is the specific heat of the flue gases, T_3 is the turbine inlet temperature, T_4 is the turbine exit temperature and w_{GT} is the net specific work of the GT.

The Steam Cycle (Rankine) and Multi-Pressure Integration. Steam generated in the HRSG replace the coal boiler output. For the HP and IP steam stages, the ST work output is calculated as [10]:

$$\dot{w}_{ST} = \sum\left(\dot{m}_{HP} \cdot (h_{HP} - h_{IP}) + \dot{m}_{IP} \cdot (h_{IP} - h_{ex})\right) \cdot \eta_{ST} \tag{6}$$

where $\dot{w}_{ST}$ is the ST work produced, $\dot{m}_{HP}$ is the HP steam mass flow, h_{HP} is the HP steam specific enthalpy, h_{IP} is the IP steam specific enthalpy, $\dot{m}_{IP}$ is the IP steam nass flow, h_{ex} is the exhaust steam specific enthalpy and η_{ST} is the ST efficiency. The heat removed from ST extractions for DH and industrial steam is calculated as [11]:

$$\dot{Q}_{DH} = (h_{IP} - h_{conden}) + (h_{LP} - h_{conden}) \tag{7}$$
$$\dot{Q}_{IS} = (h_{IP} - h_{conden}) \tag{8}$$

where $\dot{Q}_{DH}$ is the heat supplied to the DH system, h_{conden} is the condensate specific enthalpy, h_{LP} is the LP steam specific enthalpy and $\dot{Q}_{IS}$ is the heat supplied for industrial purposes. The HRSG Energy balance is calculated as [12]:

$$\dot{m}_{GT} \cdot c_f = \left(T_{ex,GT} - T_{stack}\right) = \sum \dot{m}_{steam} \cdot (h_{out} - h_{in}) \tag{9}$$

where $\dot{m}_{GT}$ is the mass flow rate of the GT exhaust gases, $T_{ex,GT}$ is the temperature of the GT exhaust entering the HRSG, T_{stack} is the temperature of the flue gas leaving the HRSG. The Exergy (Second Law) Considerations, the exergy destruction, which quantifies the irreversibilities in the system, is calculated as follows [13]:

$$\dot{E}_D = T_0 \cdot \dot{S}_{gen} \tag{10}$$

where $\dot{E}_D$ is the rate of exergy destruction, T_0 is the ambient or reference temperature and $\dot{S}_{gen}$ is the rate of entropy generation. The overall combined-cycle efficiency, accounting for both gas and steam contributions, is calculated as follows [13]:

$$\eta_{cc} = \frac{\dot{w}_{GT}+\dot{w}_{ST}}{\dot{m}_{fuel}\cdot LHV_{NG}} \tag{11}$$

where η_{cc} is the overall efficiency of the combined cycle and LHV_{NG} is the lower heating value of the fuel.

3 Results

The results are presented in the Figures below and are derived from the high-resolution operational data obtained from the plant's Supervisory Control and Data Acquisition (SCADA) system [14]. SCADA is an industrial control system used for real-time monitoring, control and data collection from processes and equipment. It acquires operational signals such as temperature, pressure, flow rates, and electrical power continuously, enabling process supervision, automated or remote control, data archiving and visualisation through Human-Machine Interfaces (HMIs). SCADA also provides alarms and notifications for abnormal conditions, supporting safe and efficient plant operation.

The SCADA infrastructure acquires and archives real-time process variables continuously (24/7/365), including the electrical power output, thermal loads, turbine control parameters and auxiliary system signals. This continuous data acquisition enables detailed performance assessment, transient analysis, and reliable validation of both thermodynamic and operational models.

The presentation of the results is based on the operation period of November 2025 and is organised sequentially. Under nominal conditions, the two GTs units exhibit similar load-following behaviour and operate in parallel within a comparable dispatch band. Deviations from parallel operation are associated primarily with abnormal or fault-induced conditions. In such cases, manual operator interventions are often required to reduce the GT load to maintain system integrity, prevent protection trips and preserve the turbine component lifetime. These deviations are clearly observable in the SCADA data as abrupt changes in electrical output, modified control setpoints and altered GT–ST interaction dynamics.

Figure 8: Electric power output of combined-cycle generators.

Fig. 8 shows the electric power generated by the GT-1, GT-2 and ST generators. During the analysed period the average power output of each gas turbine generator was approximately 54 MW, while the steam turbine generator produced around 22 MW. The Figure highlights the correlation between the ST power output and the combined output of both GTs, as all the steam generated in the HRSGs is directed to the ST. A minor temporal deviation in the response of the ST relative to the GTs can be observed, reflecting the slight delay between the changes in GT power and the resulting adjustment in the ST output.

Figure 9 shows the natural gas consumption of the combined-cycle generators, which serves as the primary fuel for plant operation. As an alternative, fuel oil may be used, or a dedicated system can inject up to 45% hydrogen into the natural gas supply. The gas consumption is expressed in normal cubic metres per hour (Nm³/h). During the analysed period, a single GT consumed on average approximately 12500

Nm³/h, resulting in a total average consumption of around 25000 Nm³/h for both GTs. The natural gas is delivered through the pipeline network at a pressure of 33 bar.

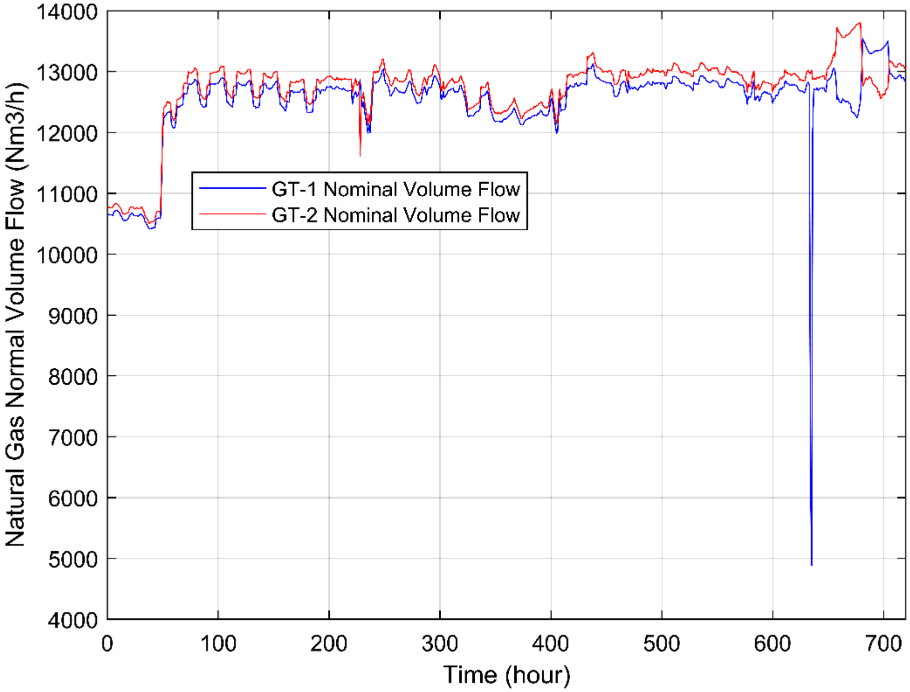

Figure 9: Natural gas consumption of combined-cycle generators.

The hot exhaust gases entering the HRSGs transfer thermal energy to the water. The mass flow rate of steam from the heat HRSGs represents the water that is evaporated and superheated within the HRSG heat exchangers, leaving the HRSGs as superheated steam. During the operation of a single GT, as shown in Fig. 8, one HRSG generates on average approximately 17 kg/s of HP steam at 90 bar and 520 °C, and about 3 kg/s of IP steam at 8,5 bar and 250 °C. The combined output from both HRSGs amounts to roughly 34 kg/s of HP steam and 6 kg/s of IP steam. The mass flow rates of steam from the HRSGs are shown in Fig. 10.

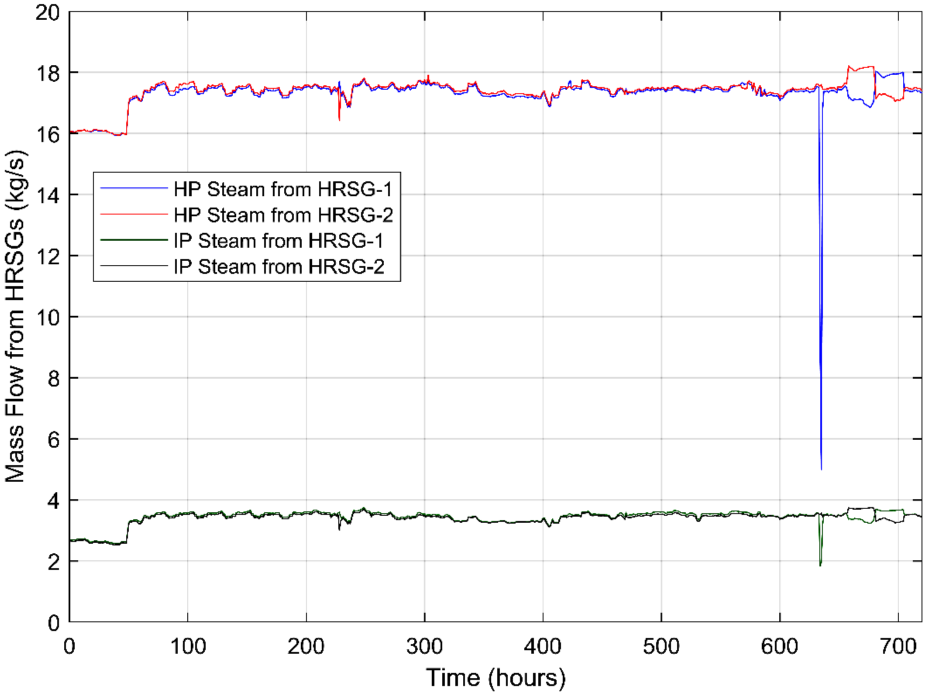

Figure 10: Mass flow rates of steam from the HRSGs.

This steam is directed to the ST, where it is converted into electrical energy at the generator, thermal energy for the district heating system and steam for industrial processes. Variations in the GT load influence the steam mass flow from the HRSGs directly, with a minor temporal delay due to the dynamics of water evaporation and superheating. These interactions are consistent with the Rankine cycle operation of the ST, highlighting the coupling between GT operation, HRSG steam generation and ST performance.

Fig. 11 presents the thermal energy supplied for a DH system and industrial purposes from the combined-cycle plant. During the analysed period, the average heat delivered to the DH network was approximately 85 MW, while the heat supplied for industrial applications averaged around 16 MW. These values reflect the distribution of steam extracted from the ST, and illustrate the combined-cycle plant's capability to provide both electrical and thermal energy, highlighting its role in the cogeneration and efficient utilisation of fuel energy.

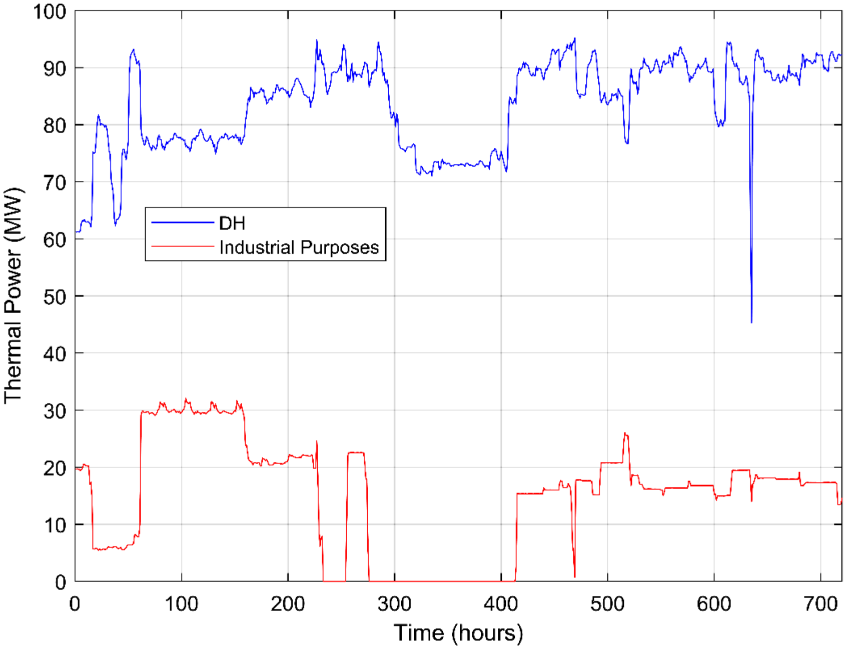

Figure 11: Heat supplied for district heating and industrial purposes from the combined-cycle plant.

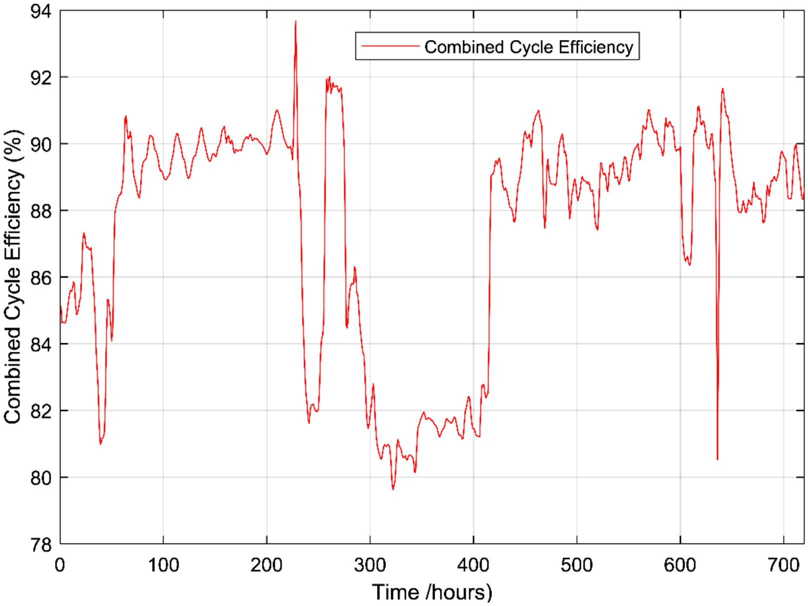

Figure 12: Combined-cycle plant efficiency.

Fig. 12 illustrates the thermodynamic efficiency of the combined-cycle plant, which ranged from 80% to 93% during the analysed period. The average efficiency over this period was approximately 87%.

The calculated results demonstrate that the combined-cycle plant operating in cogeneration mode achieves high thermodynamic efficiency, while, simultaneously, contributing to the reduction of greenhouse gas emissions. This represents a key advantage of such processes, highlighting both their energy and environmental benefits.

3 Conclusion

This study analysed the operational performance of a combined-cycle cogeneration plant retrofitted into an existing coal-fired power block, using high-resolution SCADA data collected during November 2025. The retrofit introduces a natural gas-fired GTs coupled with heat recovery steam generators HRSGs, while leveraging the existing steam turbine ST. The investigation focused on power generation, fuel consumption, steam mass flows, thermal energy delivery for district heating and industrial purposes, and overall thermodynamic efficiency.

The results indicate that both GTs units operated in parallel with similar load-following behaviour, producing on average 54 MW per unit, while the ST generated around 22 MW. The ST output followed the combined GT output closely, with minor temporal deviations due to the steam production dynamics. The natural gas consumption aligned directly with the GT load variations, averaging 12500 Nm^3/h per GT and 25000 Nm^3/h for both, delivered at a pipeline pressure of 33 bar.

The HRSGs convert exhausted heat into HP and IP steam efficiently, with combined mass flow rates of 34 kg/s of HP steam and 6 kg/s of IP steam. This steam supports electricity generation, approximately 22 MW, district heating, approximately 85 MW on average, and industrial applications, approximately 16 MW on average, demonstrating the plant's cogeneration performance and effective utilisation of recovered energy.

The thermodynamic efficiency of the combined-cycle system ranged from 80% to 93%, averaging 87%. These high efficiencies underscore the benefits of cogeneration, including optimised fuel utilisation and reduced greenhouse gas emissions. By substituting coal partially with natural gas, the retrofit achieved a meaningful reduction in CO_2 and NO_x emissions, while maintaining the operational flexibility and reliable load-following capability.

Overall, the study confirms that retrofitting a coal-fired block with a gas–steam combined cycle represents a feasible decarbonisation strategy. It leverages the existing infrastructure to achieve high energy efficiency, reduce fuel consumption and minimise the environmental impact, while maintaining a reliable power and heat supply. Future work may focus on advanced operational optimisation, predictive maintenance, and integration with variable renewable energy sources to enhance the performance, flexibility and sustainability of hybrid thermal assets further.

References

[1] Strušnik D., Avsec J., (2022). Exergoeconomic machine-learning method of integrating a thermochemical Cu–Cl cycle in a multigeneration combined cycle gas turbine for hydrogen production. *International Journal of Hydrogen Energy,* Vol. 47., Iss. 39, pp 17121-17149. https://doi.org/10.1016/j.ijhydene.2022.03.230

[2] Strušnik D., Avsec J., (2022) Exergoeconomic machine-learning method of integrating a thermochemical CueCl cycle in a multigeneration combined cycle gas turbine for hydrogen production. *International Journal of Hydrogen Energy*, Vol. 47, Iss. 39, pp 17121-17149.

[3] Strušnik D., Marčič M., Golob M., Hribernik A., Živić M., Avsec J., (2016). Energy efficiency analysis of steam ejector and electric vacuum pump for a turbine condenser air extraction system based on supervised machine learning modelling. *Applied Energy*, Vol. 173, pp 386-405. https://doi.org/10.1016/j.apenergy.2016.04.047.

[4] Strušnik D., (2021). Integration of machine learning to increase steam turbine condenser vacuum and efficiency through gasket resealing and higher heat extraction into the atmosphere. *International Journal of Energy Research* https://doi.org/10.1002/er.7375.

[5] Siemens Energy. SGT-800 gas turbine. https://www.siemens-energy.com.

[6] Strušnik D., Avsec.J., (2022). Energo economics paybeck investment calculation modelling og gas steam combined cycle power plant. *Journal of energy technology*, Vol. 15, Iss. 4, pp 11-28. https://www.dlib.si/stream/URN:NBN:SI:DOC-82E8QCOH/1e34bffc-2b36-4053-b2d5-8f3193d9e389/PDF.

[7] Abbaspour G., Ghaebi H., Ziapour B. M., Javani N., (2025). Comprehensive thermoeconomic analysis of a novel solar based multigeneration system by incorporating of S–CO2 Brayton, HRSG and Cu–Cl cycles. *International Journal of Hydrogen Energy,* Vol. 122, pp 192-205. https://doi.org/10.1016/j.ijhydene.2025.03.294.

[8] Sasmoko, Bekti A. F., Cheng P., Chen C., Tseng C., (2025). Energy and exergy analyses of protonic ceramic fuel cell/gas turbine/organic Rankine cycle hybrid systems with methanol and

octane steam reformers. *International Journal of Hydrogen Energy,* Vol. 137, pp 948-960. https://doi.org/10.1016/j.ijhydene.2024.07.325.
[9] Li K., Zhang S., (2025). Novel selective exhaust gas recirculation strategy for part-load performance of a gas turbine combined cycle with MEA-based CO2 capture. *Energy Conversion and Management,* Vol. 346, pp 120439. https://doi.org/10.1016/j.enconman.2025.120439.
[10] Vescovi G., Alpy N., Haubensack D., Azzaro-Pantel C., Stouffs P., (2025). Optimizing the flexibility of the steam Rankine cycle of an SMR for load following and cogeneration by combining a double partial arc admission for the turbine. *Energy,* Vol. 339, p 139068. https://doi.org/10.1016/j.energy.2025.139068.
[11] O'Brien S., Qureshi Z. U. A., Aghamolaei R., (2025). Comparative life cycle assessment of district heating supply pathways: Insights from waste heat and CHP configurations. *Results in Engineering,* Vol. 28, p 107718. https://doi.org/10.1016/j.rineng.2025.107718.
[12] Mehrgoo M., Amidpour M., (2025). A constructal theory framework for optimizing HRSG design: Enhancing thermal performance and cost-effectiveness. *Results in Engineering,* Vol. 27, p 105849. https://doi.org/10.1016/j.rineng.2025.105849.
[13] Ahmadi G., Jahangiri A., Toghraie D., (2023). Design of heat recovery steam generator (HRSG) and selection of gas turbine based on energy, exergy, exergoeconomic, and exergo-environmental prospects. *Process Safety and Environmental Protection,* Vol. 172, pp 353-368. https://doi.org/10.1016/j.psep.2023.02.025.
[14] SCADA system-TE-TOL Ljubljana.

Povzetek v slovenskem jeziku

Operativna in termodinamična integracija kombiniranega plinsko-parnega cikla v obstoječi premogovni blok. Ta prispevek preučuje termodinamsko integracijo kombiniranega plinsko-parnega cikla v obstoječi blok na premog z namenom zmanjšanja porabe premoga in povezanih emisij. V osnovni konfiguraciji obstoječa enota popolnoma temelji na zgorevanju mletega premoga, medtem ko retrofitna zasnova uvaja plinsko turbino na zrmrljski plin z rekuperatorjem pare. Izpušna toplota iz plinske turbine se uporablja za proizvodnjo pare za obstoječo parno turbinno, s čimer se poveča skupna učinkovitost cikla. Z ekološkega vidika zemeljski plin predstavlja bistveno nižji dejavnik emisij ogljika v primerjavi s premogom, kar povzroča sorazmeren upad emisij CO_2 in drugih toplogrednih plinov na ravni sistema. Dodatne prednosti vključujejo manjšo tvorbo NO_x zaradi čistejšega zgorevanja in izboljšano operativno fleksibilnost, kar omogoča učinkovitejše prilagajanje obremenitve ob spremenljivi integraciji obnovljivih virov. Rezultati nakazujejo, da takšna hibridizacija ponuja izvedljivo pot do dekarbonizacije termalnih virov z izkoriščanjem obstoječe infrastrukture, hkrati pa dosega pomembno zmanjšanje specifičnih emisij.

JOURNAL OF ENERGY TECHNOLOGY
Vol. 18, No. 4, pp. 231–250, December 2025

Original
Scientific
Article

EVALUATION OF THE MECHANICAL PROPERTIES OF STEEL UNDER ELEVATED TEMPERATURE CONDITIONS

KLEMEN SREDENŠEK,[1, 2] LUKA BARBIČ,[3]
ZDRAVKO PRAUNSEIS[1]

[1] University of Maribor, Faculty of Energy Technology, Krško, Slovenia
klemen.sredensek@um.si, zdravko.praunseis@um.si
[2] University of Maribor, Faculty of Electrical Engineering and Computer Science, Maribor, Slovenia
klemen.sredensek@um.si
[3] Krško Nuclear Power Plant, Krško, Slovenia
lbarbic@nek.si

CORRESPONDING AUTHOR
klemen.sredensek@um.si

Submitted
1. 12. 2025

Accepted
18. 12. 2025

Published
31. 12. 2025

Abstract This paper presents the influence of elevated temperatures on the mechanical properties of steel with varying iron content and alloying compositions. The paper combines chemical analysis and high-temperature tensile testing to examine how microstructure, chemical composition and temperature affect the yield strength, tensile strength and ductility of steel. Samples of two thicknesses (0.63 mm and 0.50 mm) and three iron levels (85 wt%, 90 wt %, and 97 wt%) were analysed and classified based on their chemical composition. Tensile tests were performed in accordance with ISO 6892-2 within the temperature range of 90 °C to 250 °C, using 20 °C increments. The findings highlight the combined effect of temperature and alloying chemistry on the high-temperature performance of steel, providing valuable insights for material selection in thermally demanding engineering applications.

Keywords
steel,
tensile test,
temperature,
chemical analysis,
stress-strain diagram,
alloying elements

https://doi.org/10.18690/jet.18.4.231-250.2025

University of Maribor Press

1 Introduction

The field of Materials Science has advanced significantly in recent years, and is becoming increasingly important in engineering and design. Numerous historical examples demonstrate that structural failures under load often occur due to inappropriate material selection [1], resulting in significant financial losses, and, in many cases, fatalities [3]. To prevent such events, a systematic study of materials and their properties began to develop. It became evident that the chemical composition and microstructure of a material determine its properties fundamentally, and that these properties are not constant under all conditions [6].

Understanding material behaviour at different temperatures is essential for the safe design of devices and structures. Many components operate in high-temperature environments or experience considerable heating during service, resulting in significant changes to their mechanical properties. If such changes are not considered properly during the design process, component failure may occur. Conversely, numerous machines and structures operate in environments exposed to low temperatures, where the risk of brittle fracture increases substantially. To prevent such unpredictable failures, the study and testing of materials became necessary. The development of standardised laboratory tests enabled reliable observation of material behaviour under various loads and environmental conditions. This knowledge enabled the selection of appropriate materials, thereby reducing the likelihood of structural failure. Continued research has also led to the development of new alloys and materials with improved properties for specific applications.

For these reasons, the paper investigates the behaviour of the mechanical properties of steel at elevated temperatures. Steel was selected as the test material because it is one of the most widely used engineering materials in industrial applications. The paper is structured into two main parts. The first part outlines the fundamental structure of metals, including their crystal structures and lattice defects, and provides an overview of steel and the key alloying elements that influence its mechanical and chemical properties. The paper also reviews the tensile test, the fundamental method for determining mechanical properties, in accordance with ISO 6892-1 for room-temperature testing and ISO 6892-2 for high-temperature testing. These Standards ensure reliable and repeatable determination of the characteristic values of metallic materials.

The aim of this paper was to determine how the mechanical properties of steel change with increasing temperature, and how they are affected by the iron content and accompanying alloying elements. These research questions guided the experimental work, which focused on tensile testing. The tests were conducted from 90 °C to 250 °C in increments of 20 °C. Before conducting the tensile tests in accordance with ISO 6892-2, a chemical analysis was performed on all the samples to verify the similarity of their chemical compositions. The samples were then categorised by thickness and iron content, resulting in five test groups.

2 Methodology

2.1 Microstructure of metals: Crystal structure, lattice defects, steel and alloying elements

When a material solidifies, it forms either an amorphous or a crystalline structure. Metals form crystalline structures almost exclusively, where the atoms are arranged in a periodic lattice described by a unit cell [7]. Most metals crystallise in one of three common structures: a face-centred cubic (FCC), hexagonal close-packed (HCP), or body-centred cubic (BCC).

The FCC structure has the highest packing density (74 %) and is characteristic of metals such as aluminium (Al), copper (Cu) and nickel (Ni). In steels, the high-temperature austenite phase also adopts the FCC structure. The HCP structure has the same packing factor but a different geometry, with each atom surrounded by twelve neighbours; this arrangement is typical of metals such as magnesium, titanium and zinc. The BCC structure has a lower packing density (68 %), with atoms touching along the body diagonal of the cube, and is found in α-iron, vanadium, niobium, tungsten and molybdenum [7].

Real crystals are never perfect. Their microstructure contains defects that affect the physical, chemical and mechanical properties significantly. Point defects, such as vacancies, interstitial atoms and substitutional atoms, play a crucial role in diffusion and high-temperature behaviour. Line defects, also referred to as dislocations, enable plastic deformation at much lower stresses than would be required in a perfect lattice

[10]. Planar defects, including stacking faults, coherent interfaces and grain boundaries, influence slip behaviour and phase transformations. Volume defects, such as porosity, inclusions and microcracks, reduce strength and fracture resistance, and are found commonly in cast products [7].

Together, the crystal structure and its defects determine the microstructure of metals and influence their mechanical behaviour significantly under various loading and temperature conditions.

Steel is an alloy of iron that contains small amounts of carbon, typically below 2.06%, together with various alloying elements that improve its mechanical, chemical and physical properties. Carbon is the most influential element, as it governs the formation of ferrite, pearlite, bainite and martensite, and affects the strength, hardness, ductility and weldability strongly. Based on their chemical composition, steels are classified as unalloyed, low-alloyed, high-alloyed, ferritic, or austenitic. By application, they are divided into tool steels, general structural steels, heat-treatable steels and special steels [8].

Austenitic steels contain elements such as manganese, nickel and cobalt, which expand the γ-phase field and stabilise the austenitic structure down to room temperature. They are non-magnetic, corrosion-resistant, and cannot be strengthened by heat treatment; their properties are improved mainly through plastic deformation. Ferritic steels contain elements such as silicon, chromium, molybdenum and titanium, which stabilise the α-phase. They are magnetic and corrosion-resistant, but, like austenitic steels, they cannot be heat-treated, and their practical significance is more limited [9].

The mechanical behaviour of steel is influenced strongly by alloying elements. Carbon increases the strength, hardness and hardenability, but reduces toughness and ductility. Manganese enhances deoxidation and hot workability, while silicon strengthens the ferrite phase and improves oxidation resistance. Elements such as chromium, nickel and molybdenum enhance corrosion resistance, hardenability and high-temperature strength, whereas vanadium, niobium and aluminium contribute to grain refinement and strengthening. Copper increases the corrosion resistance, while phosphorus and sulphur generally reduce ductility and weldability if present in higher amounts [7].

The Fe–C diagram illustrates the primary phase transformations that govern the microstructure and properties of steel. At low temperatures, iron exists as α-ferrite, a BCC phase with extremely low carbon solubility (up to 0.02 wt%) and ferromagnetic behaviour up to the Curie temperature of 768 °C. With increasing temperature, the ferrite transforms into γ-austenite, an FCC phase capable of dissolving up to 0.77 % carbon due to its more open lattice structure. At 723 °C and 0.77 wt% C, steel undergoes a eutectoid reaction, producing pearlite, a lamellar mixture of ferrite and cementite (Fe_3C). Hypoeutectoid steels form ferrite plus pearlite upon cooling, while hypereutectoid steels form pearlite together with secondary cementite. Rapid cooling of austenite produces martensite, a supersaturated and hard tetragonal phase characteristic of quenched high-carbon steels. At a higher carbon content, the system also exhibits a eutectic reaction at 1147 °C and 4.3 wt% C, where the liquid transforms into ledeburite, a mixture of austenite and cementite typical of white cast iron [5].

2.2 Tensile test methods and material response

The tensile test is the fundamental mechanical test used to determine the strength properties of materials. In this test, a sample is loaded uniaxially with a gradually increasing force, allowing determination of the elastic modulus, yield strength, tensile strength and ductility [2]. Standardised sample geometries ensure that a fracture occurs in the gauge section, while enlarged ends allow proper gripping in the testing machine. Temperature control is critical, as tensile tests may be performed at room, elevated, or reduced temperatures. Each temperature regime is governed by specific Standards that define the procedures and permissible gradients. Multiple thermocouples are often used to ensure uniform heating, since temperature variations can affect the stresses a material can withstand significantly. The testing speed also influences the measured properties. Lower strain rates generally produce lower strengths and higher ductility, while higher rates result in the opposite behaviour. Therefore, the test speed must comply with the method or product specification. During testing, the load range must match the expected values, all the measurements must be recorded carefully, and the instruments must be capable of capturing the deformation accurately. Any deviation, such as a non-linear elastic region or a sudden load drop, may indicate improper gripping, sample misalignment, or instrumentation issues. If no such problems occur, the sample is loaded until fracture, and the stress–strain curve is recorded throughout the test [4].

3 Results

This section presents the results of the chemical composition and tensile tests. To ensure the accurate and comparable evaluation of the tensile test results, a chemical analysis was first conducted to categorise the samples based on their iron content. Based on the measured values, the samples were classified into three levels of iron content (85 wt%, 90 wt%, and 97 wt%) and into two thicknesses (0.63 mm and 0.50 mm). Since the measured values varied, an acceptable deviation limit was defined of ±2 mass percent of iron. Tables 1 to 5 present the chemical composition of samples differing in iron content and thickness.

Table 1: Chemical composition of samples with 90 wt% Fe and a thickness of 0.63 mm.

	Si	Al	P	Cu	Cr	Mn	Ni	Mo	S	Ti
Sample 1	4.33	3.55	0.716	0.363	0.255	0.2	0.188	0.047	0.028	0.025
Sample 2	3.747	2.96	0.655	0.322	0.289	0.204	0.184	0.046	0.031	0.023
Sample 3	4.253	3.49	0.774	0.305	0.279	0.227	0.2	0.055	0.036	0.018
Sample 4	3.99	3.253	0.654	0.319	0.263	0.189	0.211	0.047	0.036	0.022
Sample 5	4.183	3.307	0.695	0.327	0.262	0.192	0.204	0.045	0.027	0.023
Sample 6	4.37	3.73	0.734	0.304	0.261	0.209	0.207	0.046	0.03	0.022
Sample 7	4.047	3.27	0.63	0.318	0.265	0.217	0.194	0.047	0.035	0.021
Sample 8	3.973	3.367	0.701	0.314	0.271	0.185	0.199	0.045	0.03	0.021
Sample 9	3.81	2.933	0.62	0.385	0.292	0.174	0.211	0.048	0.036	0.02
Sample 10	4.33	3.55	0.716	0.363	0.255	0.2	0.188	0.047	0.028	0.025

Table 2: Chemical composition of samples with 97 wt% Fe and a thickness of 0.63 mm.

	Si	Al	P	Cu	Cr	Mn	Ni	Mo	S	Ti
Sample 1	1.462	0	0.068	0.818	0.212	0.273	0.286	0.07	0.043	0.008
Sample 2	1.523	0	0.075	0.502	0.212	0.288	0.295	0.07	0.04	0.014
Sample 3	1.387	0	0.066	0.477	0.249	0.257	0.28	0.072	0.05	0
Sample 4	1.413	0	0.066	0.633	0.268	0.276	0.299	0.072	0.054	0.007
Sample 5	1.43	0	0.071	0.473	0.221	0.27	0.287	0.071	0.047	0.004
Sample 6	1.457	0.073	0.071	0.682	0.221	0.261	0.29	0.072	0.044	0.009
Sample 7	1.483	0	0.076	0.5	0.221	0.262	0.293	0.069	0.044	0.01
Sample 8	1.533	0	0.076	0.482	0.211	0.259	0.305	0.07	0.044	0.011
Sample 9	1.363	0	0.07	0.491	0.203	0.261	0.306	0.072	0.043	0.005
Sample 10	1.48	0	0.075	0.481	0.207	0.261	0.3	0.07	0.047	0.013

Table 3: Chemical composition of samples with 90 wt% Fe and a thickness of 0.5 mm.

	Si	Al	P	Cu	Cr	Mn	Ni	Mo	S	Ti
Sample 1	4.097	3.213	0.718	0.516	0.309	0.186	0.206	0.049	0.038	0.028
Sample 2	3.763	2.857	0.645	0.36	0.303	0.162	0.204	0.048	0.04	0.02
Sample 3	5.043	4.297	0.981	0.306	0.286	0.19	0.228	0.05	0.041	0.025
Sample 4	3.717	2.92	0.681	0.308	0.311	0.187	0.207	0.05	0.036	0.018
Sample 5	3.727	3.08	0.708	0.306	0.307	0.16	0.218	0.049	0.036	0.017
Sample 6	3.52	2.65	0.646	0.32	0.311	0.194	0.204	0.048	0.04	0.017
Sample 7	4.347	3.43	0.714	0.433	0.311	0.178	0.216	0.049	0.044	0.025
Sample 8	3.763	2.89	0.624	0.319	0.289	0.179	0.216	0.049	0.033	0.021
Sample 9	3.813	2.93	0.675	0.323	0.311	0.169	0.205	0.049	0.035	0.02
Sample 10	4.633	3.93	0.828	0.296	0.282	0.232	0.197	0.055	0.043	0.017

Table 4: Chemical composition of samples with 97 wt% Fe and a thickness of 0.5 mm.

	Si	Al	P	Cu	Cr	Mn	Ni	Mo	S	Ti
Sample 1	1.303	0.465	0.415	0.347	0.262	0.076	0.042	0.015	0.008	0
Sample 2	1.37	0.46	0.413	0.356	0.256	0.075	0.04	0.003	0.017	0.007
Sample 3	1.487	0.444	0.427	0.333	0.275	0.073	0.036	0.019	0	0
Sample 4	1.433	0.49	0.416	0.347	0.268	0.073	0.044	0.008	0	0
Sample 5	1.35	0.485	0.43	0.357	0.266	0.073	0.039	0.007	0	0.01
Sample 6	1.447	0.47	0.44	0.387	0.257	0.072	0.038	0.013	0	0
Sample 7	1.47	0.484	0.444	0.368	0.287	0.075	0.043	0.008	0	0
Sample 8	1.487	0.503	0.423	0.364	0.268	0.075	0.036	0	0.027	0
Sample 9	1.48	0.474	0.434	0.394	0.238	0.07	0.037	0.011	0	0
Sample 10	1.433	0.463	0.433	0.373	0.273	0.075	0.052	0.013	0	0

Table 5: Chemical composition of samples with 85 wt% Fe and a thickness of 0.63 mm.

	Si	Al	P	Cu	Cr	Mn	Ni	Mo	S	Ti
Sample 1	6.297	5.523	1.2	0.384	0.388	0.257	0.283	0.054	0.044	0.027
Sample 2	5.387	4.823	1.04	0.365	0.385	0.239	0.316	0.059	0.039	0.022
Sample 3	6.52	5.63	1.203	0.393	0.379	0.167	0.273	0.055	0.042	0.022
Sample 4	6.523	5.74	1.227	0.372	0.378	0.244	0.282	0.057	0.048	0.02
Sample 5	6.253	5.543	1.177	0.382	0.377	0.264	0.321	0.058	0.045	0.021
Sample 6	4.633	3.93	0.828	0.296	0.282	0.232	0.197	0.055	0.043	0.017
Sample 7	5.277	4.557	1.017	0.394	0.398	0.267	0.312	0.058	0.042	0.021
Sample 8	6.447	5.58	1.2	0.381	0.381	0.266	0.291	0.058	0.043	0.018
Sample 9	4.747	3.933	0.867	0.285	0.28	0.243	0.204	0.057	0.042	0.027
Sample 10	6.297	5.523	1.2	0.384	0.388	0.257	0.283	0.054	0.044	0.027

Tables 1 to 5 show that the chemical composition within each group of samples is highly homogeneous, as the concentrations of individual elements vary only minimally. This confirms that the material quality within each iron-content group is consistent. The Tables also reveal clear differences between the groups: samples with

97 wt% iron contain only very small amounts of other elements, whereas samples with 90 wt%, and especially 85 wt% iron, exhibit noticeably higher contents of elements such as Si, Al, Mn, or Cr. This indicates that the groups differ primarily in their degree of alloying, which will influence their mechanical behaviour in the tensile tests directly. Figure 1 presents the stress-strain diagram for samples with 90 wt% Fe and a thickness of 0.63 mm.

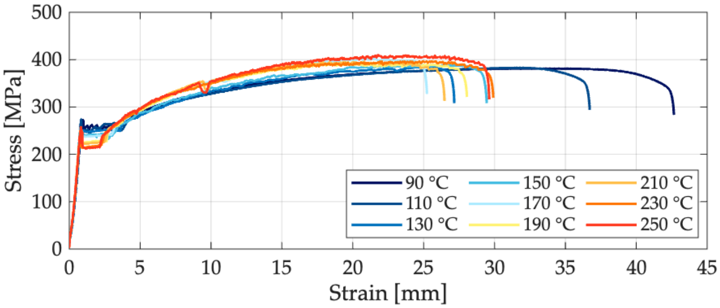

Figure 1: Stress-strain diagram for samples with 90 wt% Fe and a thickness of 0.63 mm.

Source: own.

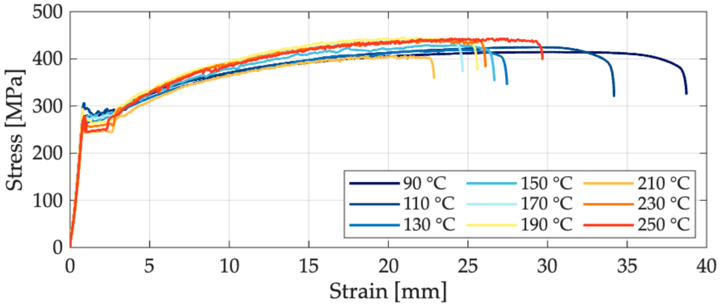

Figure 2: Stress-strain diagram for samples with 97 wt% Fe and a thickness of 0.63 mm.

Source: own.

Figure 1 shows the tensile test results for samples with 90 wt% Fe and a thickness of 0.63 mm. The measurements revealed notable differences that can be linked to the chemical composition. Sample 1, tested at 90 °C, had the lowest elastic modulus but the highest elongation, which corresponds to its low Mo content and higher Si and Ti contents. Sample 2 showed the highest elastic modulus yet the lowest tensile strength, likely due to its reduced Cr content. Sample 3 had the lowest upper yield strength in this group, while sample 4, with higher amounts of P, Mn, and Mo, reached an increased tensile strength but a noticeable drop in elongation. At intermediate temperatures (150–190 °C), variations in the alloying elements resulted in differences primarily in tensile strength and elongation. At higher temperatures (210–250 °C), the elastic modulus continued to decrease, while elongation increased gradually. The highest tensile strength was recorded at 250 °C for sample 10, which also had the highest contents of Cu, Cr, Ni, and S. Figure 2 presents the stress-strain diagram for samples with 97 wt% Fe and a thickness of 0.63 mm.

Figure 2 presents the tensile test results for samples with a composition of 97 wt% Fe and a thickness of 0.63 mm. The results revealed noticeable differences associated with the chemical composition. The sample tested at 90 °C had the lowest Fe content and the highest Cu content, which corresponded to lower tensile strength but the largest elongation in this group. At 110 °C, variations in the Mn, Fe, and Mo contents resulted in a higher yield strength and moderate changes in tensile strength and elongation. As the temperature increased to 130 °C and 150 °C, the elastic modulus rose, while the tensile strength and elongation decreased. At intermediate temperatures (170–190 °C), the samples reached similar, relatively high tensile strengths, with larger differences mainly in the elastic modulus. The sample tested at 210 °C showed the lowest tensile strength, yield strength and elongation, which aligns with its higher Si and P contents. The final samples, tested at 230 °C and 250 °C, exhibited no major differences in mechanical behaviour despite noticeable variations in their chemical composition. Figure 3 presents the stress-strain diagram for samples with 90 wt% Fe and a thickness of 0.5 mm.

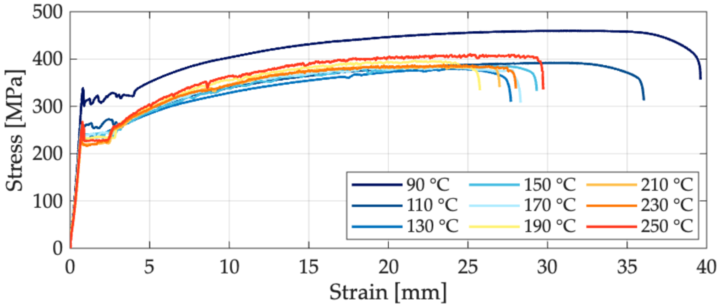

Figure 3: Stress-strain diagram for samples with 90 wt% Fe and a thickness of 0.5 mm.

Source: own.

Figure 3 shows the tensile test results for samples with 90 wt% Fe and a thickness of 0.50 mm. The sample tested at 90 °C clearly stands out, reaching the highest elastic modulus, yield strength, tensile strength and elongation, which corresponds to its higher Cu content. At 110 °C all the mechanical properties dropped sharply, due to the sample's high contents of Si, Al, P, and Mn, known to reduce strength and ductility. At 130 °C, the tensile strength and elongation decreased further. The samples tested at 150 °C and 170 °C showed almost identical behaviour, consistent with their similar chemical composition. At 190 °C, the tensile strength increased slightly, while ductility reached its lowest value because of higher P, S, and Mn contents. The samples tested at 210 °C and 230 °C reached the lowest modulus and yield strength in this group, whereas the sample tested at 250 °C showed a slight recovery in strength due to higher Ni and Mo contents. Figure 4 presents the stress-strain diagram for samples with 97 wt% Fe and a thickness of 0,5 mm.

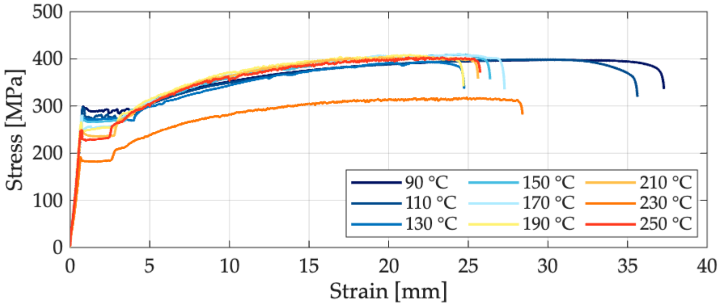

Figure 4: Stress-strain diagram for samples with 97 wt% Fe and a thickness of 0.5 mm.

Source: own.

Figure 4 shows the tensile test results for samples with 97 wt% Fe and a thickness of 0.50 mm. The sample tested at 90 °C reached the highest upper yield strength and elongation in this group, together with moderate values of elastic modulus and tensile strength. Very similar results were obtained at 110 °C and 130 °C, with only a minor increase in the elastic modulus and a more noticeable reduction in elongation at 130 °C, which aligns with their almost identical chemical compositions. At 150 °C and 170 °C, the sample exhibited very similar tensile behaviour, while sample 6 achieved the highest tensile strength and elastic modulus in this group. Between 190 °C and 230 °C, the mechanical properties decreased gradually with the increasing temperature. The sample tested at 190 °C showed the lowest elongation, and, at 230 °C, all the measured properties reached their minimum values. The chemical compositions of these samples differed only slightly. At 250 °C, sample 10 exhibited a small increase in mechanical properties, with no major differences in chemical composition compared to the others. Figure 5 presents the stress-strain diagram for samples with 85 wt% Fe and a thickness of 0.63 mm.

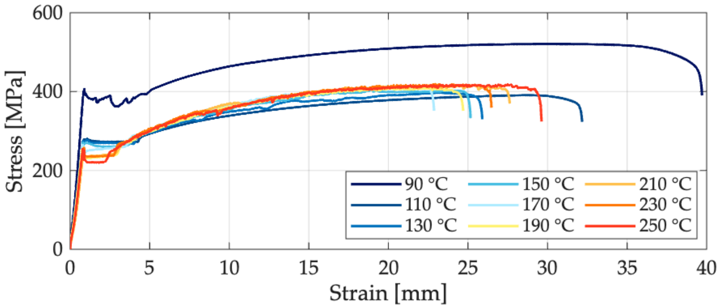

Figure 5: Stress-strain diagram for samples with 85 wt% Fe and a thickness of 0.63 mm.

Source: own.

Figure 5 shows the tensile test results for samples with 85% Fe and a thickness of 0.63 mm. The sample tested at 90 °C achieved the highest values of all the measured properties, including elastic modulus, yield strength, tensile strength and elongation. At 110 °C all the properties decreased significantly, with sample 2 showing the lowest tensile strength in this group. At 130 °C and 150 °C, the sample tested at the higher temperature exhibited a lower elastic modulus and yield strength, while the differences in elongation were minor, and tensile strength varied more noticeably. At 170 °C and 190 °C, the sample tested at the lower temperature showed the smallest elongation, whereas the difference in tensile strength was more pronounced. The samples tested at 210 °C, 230 °C, and 250 °C again showed a gradual decline in mechanical properties, with the lowest elastic modulus and yield strength recorded at 230 °C. A slight increase in tensile strength and elongation can be observed at the highest temperatures. Overall, the results indicate a clear decreasing trend in elastic modulus and yield strength with increasing temperature. Figures 6 to 10 present the stress–strain diagrams for all the samples tested at temperatures from 90 °C to 250 °C.

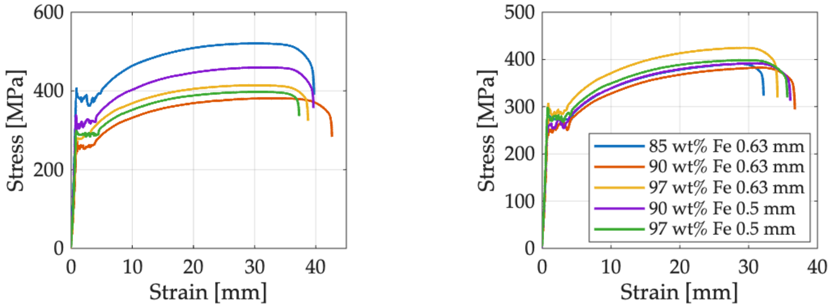

a) b)

Figure 6: Stress-strain diagram at a) 90 °C and b) 110 °C.

Source: own.

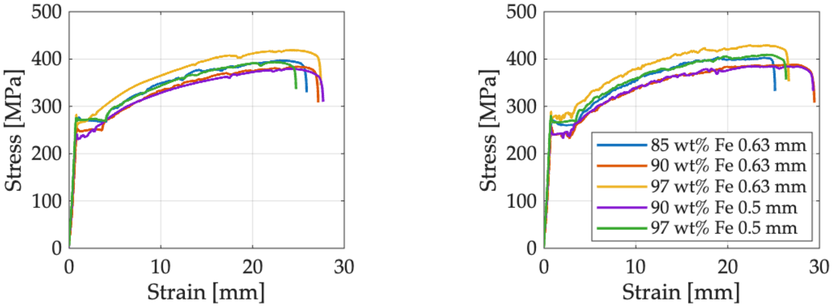

a) b)

Figure 7: Stress-strain diagram at a) 130 °C and b) 150 °C.

Source: own.

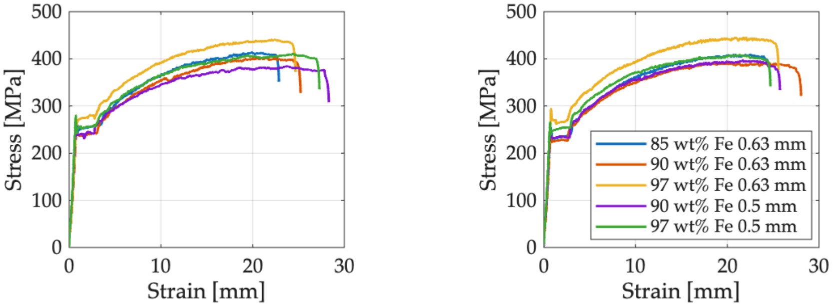

a) b)

Figure 8: Stress-strain diagram at a) 170 °C and b) 190 °C.

Source: own.

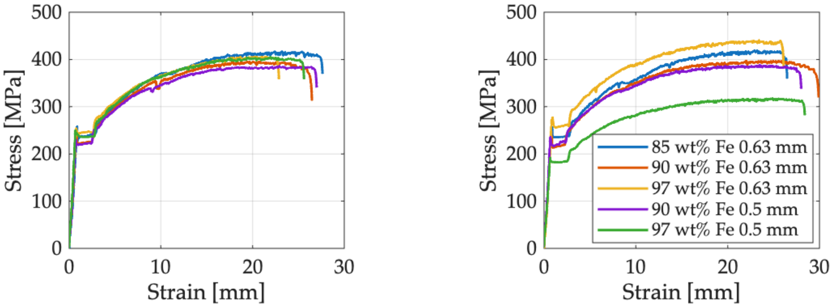

a) b)

Figure 9: Stress-strain diagram at a) 210 °C and b) 230 °C.

Source: own.

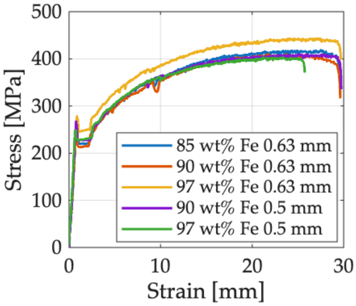

Figure 10: Stress-strain diagram at 250 °C.

Source: own.

The results presented in Figures 6 to 10 demonstrate a consistent and clearly distinguishable influence of chemical composition, particularly the Fe content and the presence of alloying elements, as well as sample thickness, on the material's mechanical response. At all the investigated temperatures, the highest values of upper yield strength and ultimate tensile strength were achieved most frequently by samples containing 97 wt% iron. These samples generally exhibited a stronger and more stable mechanical response, especially those with a thickness of 0.63 mm, which achieved the highest strength values across nearly all the temperature levels. A chemical analysis confirmed that these samples contained very low amounts of Si, P, and Al compared to the others. Since Si and Al affect solid-solution strengthening and P increases strength only in very small amounts, their reduced presence likely contributed to the more favourable mechanical behaviour. In addition, the 97 wt% Fe samples exhibited higher levels of Cu, Cr, Mn, Ni, and Mo, all of which are known to increase strength. Cr and Mo, in particular, improve high-temperature strength significantly, while Mo also enhances creep resistance. The largest elongations were recorded in the samples with 90 wt% iron, regardless of whether their thickness was 0.63 mm or 0.5 mm. The chemical compositions of these samples differed only minimally, with average deviations of approximately 0.04 ± 0.02 wt% in Si, Al, P, Cu, and Cr, and only a few thousandths of a percent in Ni, Mo, Ti, and S. These samples achieved the highest elongation values consistently, but, simultaneously, displayed some of the lowest yield strength and tensile strength values, which is consistent with the expected trade-off between strength and ductility. The lowest elongations were observed in samples with 85 wt% Fe and 0.63 mm thickness, as well as those with 97 wt% Fe and 0.5 mm thickness. These two materials differ significantly in chemical composition, sharing similarity only in their Mn and Ni content, while exhibiting substantial differences in Cu, Cr, S, Ti, Al, and Si. No single dominant factor explains their reduced elongation. The result was likely a combined effect of multiple alloying elements and microstructural interactions, amplified at elevated temperatures.

Across all the temperature ranges, a gradual decrease in yield strength, tensile strength, and elongation was observed with increasing temperature, although the selected samples exhibited local deviations due to their individual chemical compositions. The strength values were highest at 90 °C and generally decreased up to 230 °C. At 250 °C the results became more uniform, with only isolated samples showing significant deviations. The most important conclusion is that chemical composition is the dominant factor governing the mechanical response at elevated temperatures, more so than thickness alone. Samples with 97 wt% Fe and increased levels of Cr, Mo, Ni, Mn, and Cu achieved the highest strength, while samples with 90 wt% Fe exhibited the highest ductility consistently. The combined influence of individual alloying elements, not just Fe content, determines the final mechanical behaviour, and explains why samples with similar iron content can behave differently at the same temperature. Figure 11 shows the diagram of length change d_L as a function of temperature for samples with thicknesses of 0.63 mm and 0.5 mm.

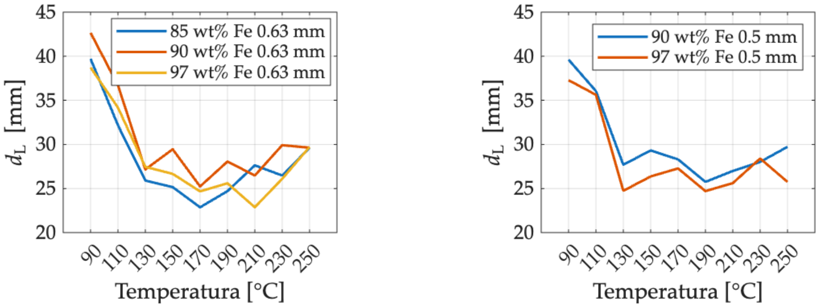

a) b)

Figure 11: Diagram of length change d_L as a function of temperature for samples with thicknesses of a) 0.63 mm and b) 0.50 mm.

Source: own.

In both cases, the highest elongations were recorded at the lowest test temperature (90 °C), after which elongation decreased consistently with the increasing temperature. Figure 11a shows the elongation of the 0.63 mm samples as a function of temperature. The highest elongations were recorded at 90 °C, ranging from 39.7 mm to 42.7 mm, after which elongation decreased steadily with the increasing temperature and stabilised between 22 mm and 30 mm. The samples containing 90 wt% Fe achieved the highest elongations across most temperatures, whereas the 85 wt% Fe samples exhibited the lowest values consistently. These differences correspond to the chemical composition: the 85 wt% Fe samples contained significantly higher P levels, which increase strength but reduce ductility. In contrast, the 90 wt% Fe samples contained more Al, which improves toughness, as well as lower Mn levels, reducing the risk of ductility loss. Small additions of Ti supported the favourable behaviour of this group further.

A similar trend was observed for the 0.50 mm samples. Figure 11b presents the elongation results for the 0.50 mm samples. As with the thicker samples, the highest elongations were obtained at 90 °C, followed by a pronounced drop between 90 °C and 130 °C. At higher temperatures, the elongation stabilised within 25–30 mm. Samples with 90 wt% Fe again achieved the highest elongations throughout the temperature range, influenced strongly by their elevated Si, Al, and P contents. The 97 wt% Fe samples showed slightly higher Cr and Ni levels, which increase strength and therefore limit elongation. Overall, the samples with higher Si contents achieved greater elongation, because Si strengthens ferrite without reducing ductility significantly, whereas an elevated P content had the opposite effect. Figure 12 shows the diagram of upper yield strength R_{eH} as a function of temperature for samples with thicknesses of 0.63 mm and 0.5 mm.

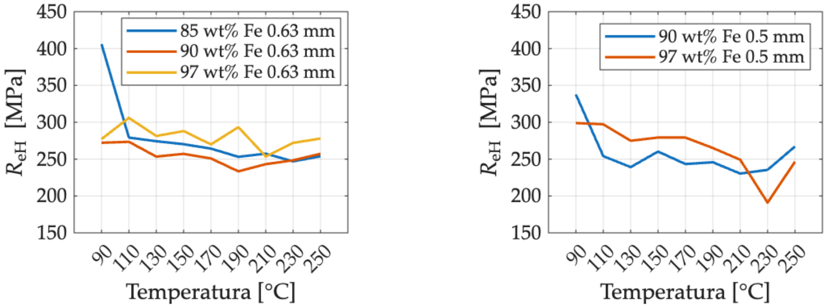

a) b)

Figure 12: Diagram of upper yield strength R_{eH} as a function of temperature for samples with thicknesses of a) 0.63 mm and b) 0.50 mm

Source: own.

Figure 12a shows the upper yield strength of the 0.63 mm samples as a function of temperature. The results indicate that samples containing 97 wt% Fe achieved the highest yield strength values consistently. At 90 °C, the differences between the samples were more pronounced, while, at higher temperatures, the values converged gradually and remained within 230–305 MPa. A general downward trend of yield strength with increasing temperature was evident. The chemical analysis helps explain these trends. The 97 wt% Fe samples contained the lowest amounts of Si and P, elements known to reduce ductility and toughness when present in higher concentrations. These samples also showed slightly elevated Mo contents, which is consistent with their improved high-temperature strength. The samples with 90 wt% Fe reached the lowest yield strength values across the full temperature range. Their results were comparable to those of the 85 wt% Fe group, which is consistent with their similar levels of Cu, Cr, Mn, Mo and S.

Figure 12b presents the results for the 0.50 mm samples. As observed for the thicker group, samples with 97 wt% Fe generally achieved the highest yield strength values. More noticeable deviations occurred at 90 °C and 230 °C, where the 90 wt% Fe sample reached slightly higher values than expected. Across all the samples a clear decline in yield strength was observed as the temperature increases. The elevated values of the 97 wt% Fe samples correlated with their higher contents of Cu, Cr, Ni, and Mo, elements known to enhance strength and hardness. These samples also contained significantly less S, which, typically, appears as sulphide inclusions and affects ductility adversely. In contrast, the 90 wt% Fe samples exhibited two- to three-fold higher Si and elevated P levels, both of which can increase strength, but reduce ductility when present in excessive amounts. Figure 13 shows the diagram of maximum tensile strength R_m as a function of temperature for samples with thicknesses of 0.63 mm and 0.5 mm.

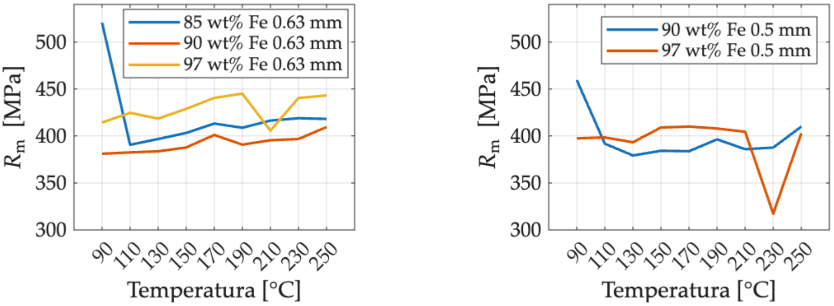

a) b)

Figure 13: Diagram of maximum tensile strength R_m as a function of temperature for samples with thicknesses of a) 0.63 mm and b) 0.50 mm

Source: own.

Figure 13a shows the tensile strength of samples with a thickness of 0.63 mm at different testing temperatures. On average, the samples containing 97 wt% Fe achieved the highest tensile strength. A notable deviation occurred only at 90 °C, where the 85 wt% Fe samples reached 520 MPa. With increasing temperature, the results stabilised between 380 MPa and 450 MPa, and the overall average tensile strength for this thickness was approximately 414 MPa. The chemical analysis revealed that the 97 wt% Fe samples contained the lowest concentrations of Si and P. Since P can reduce ductility and toughness significantly when present in larger amounts, its low content is consistent with the higher observed tensile strength. These samples contained practically no Al, but showed slightly elevated Mo levels, which are known to enhance tensile strength at elevated temperatures. The 90 wt% Fe samples exhibited the lowest tensile strength consistently across the entire temperature range, with values comparable to those of the 85 wt% Fe group. Their chemical composition showed similar contents of Cu, Cr, Mn, Mo, and S. A slightly higher Ti content was observed in the 85 wt% Fe group, which generally increases strength and hardness. More pronounced differences were found in Si, Al, and P, all present in higher concentrations in the 90 wt% Fe samples.

Figure 13b shows the tensile strength of samples with a thickness of 0.5 mm. As before, the 97 wt% Fe samples achieved the highest values in most tests, except at 90 °C, where the 90 wt% Fe sample reached 460 MPa. A more noticeable drop occurred for the 97 wt% Fe sample at 230 °C. Compared to the 0.63 mm group, the reduction in tensile strength with increasing temperature was less pronounced. The higher strength of the 97 wt% Fe samples is supported by their increased contents of Cu, Cr, Ni, and Mo. These alloying elements enhance hardness and tensile strength significantly. This group also contained substantially less S, which, typically, appears as sulphide inclusions, and can influence mechanical performance negatively. The Mn and Ti contents were similar between the chemical groups, while the Si levels in the 90 wt% Fe samples were two to three times higher. Al was not detected in the 97 wt% Fe samples.

5 Conclusion

This paper examined the mechanical behaviour of steel with varying iron contents and alloying compositions at elevated temperatures. The combined evaluation of chemical composition and high-temperature tensile testing showed that temperature and alloying chemistry determine the material's strength and ductility jointly. Samples containing 97 wt% Fe achieved the highest yield strength and tensile strength consistently across most temperatures. Their favourable behaviour is linked to the low contents of Si, P, and Al and slightly higher amounts of Cr, Mo, Ni, Mn, and Cu, all of which improve high-temperature strength. In contrast, the samples with 90 wt% Fe exhibited the highest ductility, due primarily to their higher Si and Al contents and lower Mn levels. The lowest elongations were observed in the 85 wt% Fe samples and in the thinner 97 wt% Fe samples, reflecting the combined influence of multiple alloying elements rather than a single dominant factor.

Temperature had a clear and consistent effect: the yield strength, tensile strength, and elongation decreased with the increasing temperature, with the greatest differences observed at 90 °C, and progressively smaller differences observed as the temperature increased toward 250 °C. At higher temperatures, the mechanical response became more uniform, regardless of thickness. Overall, the results indicate that the chemical composition is the primary factor governing mechanical behaviour at elevated temperatures, while sample thickness plays a secondary role. These findings provide a useful basis for selecting steel grades for thermally demanding applications, where the balance between strength and ductility depends on the combined effects of specific alloying elements.

Acknowledgment

The authors acknowledge the use of research equipment, a Temperature test chamber and a Module for fast X-ray spectral chemical analysis of materials, procured within the operation "Upgrading national research infrastructures - RIUM", which was co-financed by the Republic of Slovenia and the European Union from the European Regional Development Fund.

References

[1] Brnic, J., Turkalj, G., Canadija, M., Lanc, D., & Brcic, M. (2015). Study of the Effects of High Temperatures on the Engineering Properties of Steel 42CrMo4. *High Temperature Materials and Processes*, *34*(1), 27–34. https://doi.org/10.1515/htmp-2014-0011

[2] Chen, X., Lu, J., Lu, L., & Lu, K. (2005). Tensile properties of a nanocrystalline 316L austenitic stainless steel. *Scripta Materialia*, *52*(10), 1039–1044. https://doi.org/10.1016/j.scriptamat.2005.01.023

[3] Grässel, O., Krüger, L., Frommeyer, G., & Meyer, L. (2000). High strength Fe-Mn-(Al, Si) TRIP/TWIP steels development - properties - application. *International Journal of Plasticity*, *16*(10-11), 1391–1409. https://doi.org/10.1016/s0749-6419(00)00015-2

[4] Liang, Z., Wang, W., & Wang, Z. (2022). Effect of cold-form and tensile strain rate on mechanical properties of Q345 steel at elevated temperatures. *Journal of Constructional Steel Research*, *191*, Article 107192. https://doi.org/10.1016/j.jcsr.2022.107192

[5] Liu, X., Lan, S., & Ni, J. (2014). Analysis of process parameters effects on friction stir welding of dissimilar aluminum alloy to advanced high strength steel. *Materials & Design*, *59*, 50–62. https://doi.org/10.1016/j.matdes.2014.02.003

[6] Nikulin, I., Kipelova, A., & Kaibyshev, R. (2012). Effect of high-temperature exposure on the mechanical properties of 18Cr-8Ni-W-Nb-V-N stainless steel. *Materials Science and Engineering a-Structural Materials Properties Microstructure and Processing*, *554*, 61–66. https://doi.org/10.1016/j.msea.2012.06.011

[7] Reardon, A. C. (2011). *High temperature tensile behavior of carbon steels* (Second ed.). ASM International.

[8] Schneider, M., & Laplanche, G. (2021). Effects of temperature on mechanical properties and deformation mechanisms of the equiatomic CrFeNi medium-entropy alloy. *Acta Materialia*, *204*, Article 116470. https://doi.org/10.1016/j.actamat.2020.11.012

[9] Sohn, S., Hong, S., Lee, J., Suh, B., Kim, S., Lee, B., Kim, N., & Lee, S. (2015). Effects of Mn and Al contents on cryogenic-temperature tensile and Charpy impact properties in four austenitic high-Mn steels. *Acta Materialia*, *100*, 39–52. https://doi.org/10.1016/j.actamat.2015.08.027

[10] Verhoeven, J. D. (2007). *High temperature tensile behavior of carbon steels.* ASM International.

Povzetek v slovenskem jeziku

Analiza mehanskih lastnosti jekla pri povišanih temperatura. Članek predstavlja vpliv povišanih temperatur na mehanske lastnosti jekla z različno vsebnostjo železa in legirnimi dodatki. V raziskavi so združeni kemijska analiza in natezni preizkusi pri povišanih temperaturah z namenom preučitve vpliva mikrostrukture, kemijske sestave in temperature na mejo tečenja, natezno trdnost in duktilnost jekla. Analizirani in razvrščeni so bili vzorci dveh debelin (0,63 mm in 0,50 mm) ter treh vsebnosti železa (85 mas. %, 90 mas. % in 97 mas. %), glede na njihovo kemijsko sestavo. Natezni preizkusi so bili izvedeni v skladu s standardom ISO 6892-2 v temperaturnem območju od 90 °C do 250 °C, v korakih po 20 °C. Rezultati poudarjajo skupni vpliv temperature in legirne kemije na obnašanje jekla pri povišanih temperaturah ter zagotavljajo dragocene usmeritve za izbiro materialov v termično zahtevnih inženirskih aplikacijah.

JOURNAL OF ENERGY TECHNOLOGY
Vol. 18, No. 4, pp. 251–260, December 2025

ENVIRONMENTAL ASSESSMENT: SAFEGUARDING NATURE AND ACCELERATING THE GREEN TRANSITION

Professional Article

Submitted
1. 12. 2025

Accepted
23. 12. 2025

Published
31. 12. 2025

MATEJ FIKE, MARKO PEZDEVŠEK, ANDRAŽ ROGER
niversity of Maribor, Faculty of Energy Technology, Krško, Slovenia
matej.fike@um.si, marko.pezdevsek@um.si, andraz.roger@um.si

CORRESPONDING AUTHOR
matej.fike@um.si

Abstract The accelerated deployment of a renewable energy infrastructure is a cornerstone of the European green transition, yet the planning, assessment and permitting processes are perceived increasingly as bottlenecks. This paper examines environmental assessment as an enabling framework that can support faster, more coherent and more legitimate decision-making in the context of energy system transformation. Rather than framing environmental assessment as a procedural barrier, the paper conceptualises it as a decision-making and governance infrastructure that integrates environmental, social and health considerations into energy planning. Drawing on recent research and a synthesis of contemporary practice, the paper highlights the importance of early engagement, systems thinking and transformative approaches that move beyond narrow compliance-oriented assessment. Particular attention is given to the balance between acceleration and simplification, as well as to the role of agency, collaboration and professional capacity. The paper concludes that a well-designed environmental assessment does not slow down the green transition, but helps ensure that it is resilient, legitimate and aligned with the long-term sustainability objectives.

Keywords
environmental assessment, green energy transition, Environmental Impact Assessment (EIA), Strategic Environmental Assessment (SEA), sustainable development goals, systems thinking, energy planning and governance

---

https://doi.org/10.18690/jet.18.4.251-260.2025

University of Maribor Press

1 Introduction

The accelerated deployment of renewable energy technologies has become a defining feature of the European green transition. Wind farms, solar power plants, power-to-X facilities, carbon capture and storage, grid reinforcements and large-scale infrastructure projects are being developed at an unprecedented pace in response to climate targets and energy security concerns. While technological solutions and investment readiness have advanced rapidly, the institutional capacity has struggled to keep up. The planning, assessment and permitting processes are identified increasingly as critical bottlenecks – not necessarily due to their existence, but due to their ability to balance speed, sustainability and societal legitimacy [1].

Within this debate, environmental assessment is often framed as a procedural constraint that slows down project implementation. Such a perception, however, risks overlooking the core function and potential of an environmental assessment. When applied with purpose and at the right stage, an environmental assessment can operate as an enabling governance mechanism that helps translate technological readiness into responsible and legitimate action. Rather than acting as a brake on development, it can function as a bridge between urgency and responsibility – supporting decisions that are not only fast, but also fair and sustainable [1].

This perspective aligns with the recent environmental assessment scholarship, which emphasizes increasingly the need to move beyond narrow compliance-oriented practices towards more decision-oriented and transformative approaches.

The environmental assessment encompasses a broader family of impact assessment instruments, including the Environmental Impact Assessment (EIA) at the project level and Strategic Environmental Assessment (SEA) at the level of plans and programs. Embedded in the European Directives, the ESPOO Convention and its SEA Protocol, these instruments form a cornerstone of environmental governance across Europe and globally. Their scope is deliberately broad, extending beyond biophysical impacts to include the population, human health, land use, material assets and cumulative effects. This requires systems thinking – an ability to recognize interconnections, trade-offs and synergies between climate mitigation, biodiversity protection, resource use and social well-being. A narrow focus on carbon reduction alone risks shifting environmental and social burdens elsewhere, thereby undermining the long-term resilience of the transition [1] [2] [3].

Recent research has highlighted the importance of rethinking both the role and the timing of environmental assessment. Early engagement, particularly through effective scoping, is critical for shaping alternatives, avoiding technological and spatial lock-ins and reducing conflicts later in the project lifecycle. Studies have demonstrated that integrating broader sustainability objectives – such as those articulated through the United Nations Sustainable Development Goals - can strengthen the relevance and completeness of environmental assessments, especially with regard to human health and social dimensions [2] [4].

At the same time, current policy debates emphasize the need for accelerated permitting and regulatory simplification to meet the 2030 and 2050 targets. While simplification can improve efficiency and quality when applied thoughtfully, it can also weaken environmental protection, public participation and trust if pursued in a narrow or reductive manner.

Against this background, this paper examines environmental assessment as an enabling framework for the sustainable green energy transition. The paper explores how environmental assessment can support faster, more coherent and more legitimate decision-making without compromising its safeguarding role. Rather than presenting new empirical findings, the contribution offers a conceptual and integrative perspective aimed at energy planners, engineers, policymakers and practitioners operating at the intersection of technology, governance and sustainability.

2 Environmental Assessment in the Green Energy Transition

Environmental assessment is situated at the intersection between energy system transformation and environmental governance. In the European context, nearly all key elements of the green energy transition – renewable energy installations, grid expansion, power-to-X facilities, carbon capture and storage, as well as large-scale spatial planning initiatives - fall within the scope of the Environmental Impact Assessment (EIA) or Strategic Environmental Assessment (SEA) [1].

As such, environmental assessment represents a critical interface where technological ambitions meet regulatory frameworks, societal values and ecological limits. Rather than functioning solely as a protective mechanism, environmental assessment plays a broader role in risk management, optimization and legitimacy-building. By identifying environmental and social risks early, shaping alternatives and informing decision-making processes, the assessment can support projects in navigating complex real-world conditions. This role is particularly relevant in the context of rapid renewable energy deployment, where conflicts over land use, biodiversity, local communities and cumulative impacts are increasingly common. Environmental assessment offers a structured arena in which these competing interests can be addressed transparently and systematically, thereby reducing the likelihood of downstream opposition and project delays.

3 Environmental Assessment as a Decision-Making and Systems Framework

At its core, an environmental assessment is not an end in itself, but a means to support informed decision-making. Its purpose is to ensure that choices, whether at the level of policy, planning or project development, are made with knowledge rather than in ignorance. This requires a systems perspective that recognizes the interconnected nature of the environmental, social and economic dimensions of sustainability.

A narrow focus on climate mitigation alone risks creating unintended consequences. Large renewable energy projects may deliver significant carbon reductions while simultaneously degrading biodiversity, altering landscapes, or displacing local communities. The research emphasizes that sustainability cannot be reduced to a single objective, instead, it involves navigating trade-offs across multiple boundary conditions [3].

An environmental assessment provides an institutionalized space where these trade-offs can be examined, negotiated, and, where possible, transformed into synergies. The integration of human health and broader social considerations strengthens the relevance of environmental assessment further. Expanding the scope of EIA and SEA beyond the traditional biophysical parameters enables a more comprehensive understanding of project impacts and aligns assessment practice with the wider sustainability objectives [2]. In this sense, environmental assessment functions as a systems-based decision framework rather than a technical checklist.

4 From Mitigation to Enhancement: Rethinking the Role of Environmental Assessment

Environmental assessment has traditionally been structured around the mitigation hierarchy, prioritizing impact prevention, followed by minimization, restoration and compensation. While this hierarchy remains a fundamental principle, recent research has highlighted the limitations of a purely compliance-oriented application. Increasingly, assessment practice is evolving towards more proactive and transformative approaches, that seek not only to reduce harm, but also to generate positive environmental and social outcomes.

The concept of "beyond compliance" reflects a shift towards enhancement and transformative mitigation strategies, particularly in the context of biodiversity and spatial planning [3]. Within this perspective, development projects are no longer viewed solely as sources of impact, but also as opportunities to contribute to ecological restoration, social cohesion and long-term resilience. Environmental assessment can play a key role in enabling such outcomes, by reframing how alternatives are developed and evaluated, and by encouraging innovation within the project design.

5 Acceleration and Simplification: Maintaining Fitness for Purpose

The urgency of the green transition has placed increasing pressure on regulatory systems to accelerate the permitting and approval processes. Across Europe, reforms aimed at shortening timelines, improving digitalization and streamlining administrative procedures are being introduced, to support faster deployment of a renewable energy infrastructure [1]. While such measures can enhance efficiency, simplification remains a contested concept. Simplification can take multiple forms, including regulatory changes, administrative streamlining and improvements in assessment practice through better data, methods and digital tools. When applied wisely, these measures can improve both the speed and quality of environmental assessment. However, oversimplification carries significant risks. Reducing the scope of assessment too narrowly may weaken the environmental protection, limit public participation and erode trust, ultimately increasing the likelihood of legal challenges and social resistance.

Research on EIA scoping demonstrates that early-stage decisions about what issues are considered, and which are excluded, have far-reaching implications for project outcomes and societal acceptance [4].

Maintaining fitness for purpose therefore requires a careful balance between acceleration and integrity, ensuring that simplification enhances, rather than undermines, the sustainability objectives.

6 Agency, Actors and Collaboration in Environmental Assessment

The environmental assessment processes are shaped not only by formal procedures and instruments, but also by the actions and interactions of multiple actors. Authorities, developers, consultants, researchers, non-governmental organizations and local communities all play distinct roles in shaping the assessment outcomes. As such, the environmental assessment is both a technical and a democratic process, dependent on collaboration, transparency and trust.

The recent scholarship emphasizes that meaningful change requires collective agency. Tools, regulations and methodologies only become effective when the actors possess the competence, confidence and willingness to use them constructively. Capacity building, professional networks and shared guidance frameworks can strengthen this collective agency by aligning the expectations and practices across the sectors [3].

In the context of the green energy transition, such collaboration is essential for ensuring that environmental assessment remains a facilitating agent rather than a procedural obstacle.

7 Discussion: Environmental Assessment as an Enabling Infrastructure

The analysis presented in this paper supports a reframing of environmental assessment from a procedural requirement towards an enabling infrastructure for the green energy transition. Rather than constituting an external constraint imposed on energy projects, environmental assessment operates at the core of the decision-making processes where technological ambitions, environmental limits and societal values intersect. When applied early, coherently and with a systems perspective, an environmental assessment can reduce uncertainty, improve project design and enhance legitimacy, thereby contributing to a more robust and timely implementation of the energy infrastructure. A central insight emerging from both practice and recent research is that many delays attributed to environmental assessment are not caused by the assessment itself, but by its late or fragmented application. Reactive assessments, introduced after key strategic decisions have already been made, tend to trigger conflict, legal challenges and public opposition. In contrast, early-stage engagement through strategic environmental assessment and well-designed scoping processes can help steer development away from environmentally and socially sensitive areas, reducing the downstream risks and increasing the predictability for developers and authorities alike [4].

The discussion on acceleration and simplification highlights further that speed and sustainability are not inherently incompatible. Simplification measures can improve efficiency and quality when they focus on better coordination, improved data availability, digital tools and enhanced professional competence. However, simplification that prioritizes speed at the expense of participation, transparency or environmental protection risks undermining the very objectives of the green transition. Such approaches may lead to short-term gains, but often result in long-term setbacks through loss of trust, increased litigation and weakened social acceptance.

Environmental assessment also plays a critical role in addressing the multi-dimensional nature of sustainability. By integrating biodiversity, human health and social considerations alongside climate objectives, the assessment processes help avoid narrow optimization strategies that shift burdens across the environmental or societal boundaries. Recent research has demonstrated that incorporating broader sustainability frameworks, such as the Sustainable Development Goals, strengthens the relevance of the environmental assessment and enhances its capacity to support transformative change [2] [3].

In this sense, environmental assessment functions as a mediating space, where trade-offs are made explicit and more balanced decisions can emerge.

Finally, the effectiveness of an environmental assessment depends fundamentally on the agency. Instruments, methodologies and regulations do not operate in isolation, they are enacted by people. Collective agency - expressed through collaboration between authorities, developers, experts and communities - is essential for translating the assessment frameworks into meaningful outcomes. Capacity building, shared standards and professional leadership can strengthen this collective agency, ensuring that the environmental assessment evolves in step with the demands of the green energy transition.

8 Conclusions and Implications for Energy Planning and Policy

This paper has examined environmental assessment as an enabling framework for the sustainable green energy transition. Drawing on recent research and a synthesis of contemporary practice, it has shown that environmental assessment is not inherently a barrier to rapid deployment of renewable energy and related infrastructure. On the contrary, when applied strategically and with purpose, an environmental assessment can support faster, more coherent and more legitimate decision-making.

Three core conclusions can be drawn. First, timing matters. An early-stage environmental assessment, particularly at the strategic and scoping levels, is decisive for shaping viable alternatives, avoiding lock-in effects and reducing conflict. Second, sustainability requires a systems perspective. Addressing climate objectives in isolation risks undermining biodiversity, human health and social cohesion. The environmental assessment provides an institutionalized mechanism for navigating these interdependencies and aligning energy development with the broader sustainability goals. Third, people matter as much as tools. The effectiveness of an environmental assessment depends on the collective agency, professional competence and collaboration across sectors.

For energy planning and policy, these insights imply that efforts to accelerate the green transition should focus not on weakening environmental assessment, but on strengthening its enabling capacity. This includes investing in early strategic planning, improving coordination across the regulatory frameworks, supporting digitalization and data sharing, and enhancing education and professional networks.

Simplification should be pursued wisely, with an emphasis on improving quality and efficiency rather than reducing the scope or participation.

In conclusion, an environmental assessment can serve as one of the critical bridges between urgency and responsibility in the green energy transition. Done right, it does not slow progress, instead, it helps ensure that progress is durable, legitimate and aligned with the long-term sustainability objectives. As energy systems continue to transform at scale and speed, the role of the environmental assessment as an enabling infrastructure will remain central to achieving a transition that is not only fast, but also fair.

References

[1] Kørnøv, Lone. (2025). Environmental Assessment as a Catalyst for Sustainable Energy Transitions: Overcoming Bottlenecks through Innovation and Change Agency.

[2] Gulis, G., Krishnankutty, N., Boess, E. R., Lyhne, I., & Kørnøv, L. (2022). Environmental Impact Assessment, Human Health and the Sustainable Development Goals. *International Journal of Public Health, Volume 67 - 2022*. doi:10.3389/ijph.2022.1604420

[3] Kørnøv, Lone, Boess, Emilia Ravn, Eliasen, Søren Qvist, Larsen, Sanne Vammen, Locher-Krause, Karla E., Zhu, Yuanzao, . . . Partidario, Maria Rosario. (2025). Beyond compliance: Enhancing biodiversity through transformative mitigation strategies in spatial planning related SEAs and EIAs. *Environmental Impact Assessment Review, 114*, 107960. doi:https://doi.org/10.1016/j.eiar.2025.107960

[4] Ravn Boess, Emilia, Lyhne, Ivar, Davila, Juanita Gallego, Jantzen, Emilie, Kjellerup, Ulf, & Kørnøv, Lone. (2021). Using Sustainable Development Goals to develop EIA scoping practices: The case of Denmark. *Impact Asse*

Povzetek v slovenskem jeziku

Presoja vplivov na okolje: Varovanje narave in pospešitev zelenega prehoda. Pospešeno uvajanje infrastrukture za obnovljivo energijo je temelj evropskega zelenega prehoda, vendar se postopki načrtovanja, presoje in izdaje dovoljenj vse bolj dojemajo kot ozka grla. Ta članek obravnava presojo vplivov na okolje kot omogočitveni okvir, ki lahko podpira hitrejše, bolj usklajeno in bolj legitimno odločanje v kontekstu preobrazbe energetskega sistema. Namesto da bi presojo vplivov na okolje predstavljali kot postopkovno oviro, jo članek konceptualizira kot infrastrukturo za odločanje in upravljanje, ki v energetsko načrtovanje vključuje okoljske, družbene in zdravstvene vidike. Na podlagi nedavnih raziskav in sinteze sodobne prakse članek poudarja pomen zgodnjega vključevanja, sistemskega razmišljanja ter transformativnih pristopov, ki presegajo ozko na skladnost usmerjeno presojo. Posebna pozornost je namenjena ravnotežju med pospeševanjem in poenostavljanjem ter vlogi agencije, sodelovanja in strokovne usposobljenosti. Članek sklene, da dobro zasnovana presoja vplivov na okolje ne upočasnjuje zelenega prehoda, temveč pomaga zagotoviti, da je odporen, legitimen in usklajen z dolgoročnimi cilji trajnosti.

University of Maribor

Faculty of Energy Technology

https://journals.um.si/index.php/jet

jet@um.si

ISSN 2463-7815 (electronic)
ISSN 1855-5748 (printed)

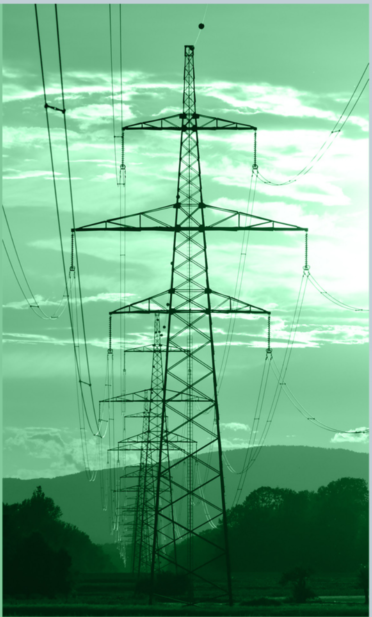

JET